UNIVERSITY
OF TRENTO - Italy
DEPARTMENT OF INDUSTRIAL ENGINEERING

XXVII cycle

Doctoral School in Materials Science and Engineering

Powder metallurgy: investigation of metallurgical and technological aspects and potential applications for critical components of turbomachineries

Piergiorgio Stella

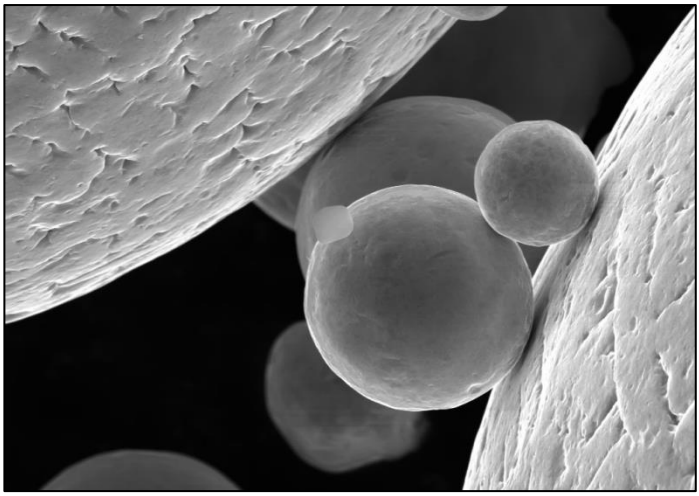

March 2016

Powder metallurgy: investigation of metallurgical and technological aspects and potential applications for critical components of turbomachineries

Piergiorgio Stella
E-mail: Piergiorgio.stella@unitn.it

Approved by:
Prof. Alberto Molinari, Advisor
Department of Industrial Engineering
University of Trento*, Italy.*

Ph.D. Commission:
Prof.ssa Ilaria Cristofolini,
Department of Industrial Engineering
University of Trento*, Italy.*

Prof. Paolo Antonio Netti,
Department of Chemical, Materials and Production Engineering
University of Naples*, Italy.*

Prof. Maurizio Vedani,
Department of Department of Mechanical Engineering
Politecnico di Milano, Italy.

University of Trento,
Department of Industrial Engineering

March 2016

A ML

Abstract

The application of powder metallurgy (PM) technologies to the manufacturing of Oil & Gas turbomachineries' components was investigated in the course of research collaboration with the *Material and Processes Engineering* Department of *General Electric Oil & Gas* (Italy). The thesis focused on the study of the pressure-assisted Hot Isostatic Pressing technology for the processing of the corrosion resistant Ni-base alloy N07626.

The densification behaviour of the N07626 metal powder in condition of pressure assisted sintering was investigated by experiments conducted on a small scale by uniaxial hot pressing condition using a Spark Plasma Sintering (SPS) machine in the aim of extending the result to the initial stage of densification of HIP. The SPS exepriments demonstrated that the densification rate is strongly affected by the process temperature and it is less sensitive to the variation of applied pressure.

The microstructure and mechanical properties of full-dense HIPped N07626 alloy, produced according to a fixed proprietary cycle and several experimental deviations were analyzed. The microstructure was studied by Optical Metallography, Scanning Electron Microscopy, Energy Dispersed X-Ray Spectroscopy and Electron Backscatter Diffraction. The mechanical properties of the alloy were assessed by tensile testing, conventional and instrumented Charpy V-Notch testing, J_{IC} fracture toughness tests and fatigue crack growth rate testing.

The tensile and impact toughness properties resulted sensitive to the local accumulation of oxygen in Oxygen Affected Zones (OAZs), that leads to a ductile to brittle transition in the impact toughness of the material. Two models for formation of OAZs were proposed based on the phase transformation and the oxidation/reduction reactions taking place in the HIP. The mechanical properties were discussed on the base of the microstructure of the Prior Particle Boundaries (PPBs) interface, focusing of the phase transformation products, represented by a thin layer of submicrometric oxides and carbides. The fracture mode was explained by the analogy with models of ductile micro-mechanisms of void nucleation and coalescence and with fracture models of particulate reinforced metal-matrix-

composite. The Charpy impact toughness and the fracture toughness were correlated to the oxygen concentration and to the density of inclusions. The fatigue crack propagation behavior was discussed focusing on the effect of clustering of inclusions on the crack propagation path. A relation between the Paris slope with the impact toughness was found. Finally the increase of processing temperature (HIP and heat treatment) was found significanty beneficial for the toughness. This effect was investigate by grain-size analysis and was proposed to be related to a reduction of density of PPBs inclusions.

Table of contents

Chapter I

Powder metallurgy technologies for critical components of Oil & Gas Turbomachineries

1.1 - Introduction

There are many reasons to introduce powder metallurgy into the manufacturing processes of industries producing turbomachineries for the Oil & Gas market. The benefits of such introduction range from an intrinsic improvement of the physical and mechanical properties of the materials used, to new design capabilities made possible by novel geometrical complexity, to a dramatic optimization of the current machining practices through a dramatic saving of raw material to remove. These benefits apply also to the most critical components of O&G Turbomachineries, whose failure would cause an onerous loss of production and also serious impact for the safety of the workers and of the environment.

This work presents part of the results of research activities conducted during the PhD in collaboration with the *Materials and Processes Engineering* department of *General Electric Oil & Gas (Italy)* concerning the introduction of powder metallurgy (P/M) technologies for the manufacturing of components for several turbomachineries for the Oil & Gas market. These activities investigated the application of two P/M technologies, pressure-assisted sintering and Additive Manufacturing by 3D laser printing, to the processing of three categories of metallic alloys: Ni-base superalloys, titanium alloys and stainless steel. The thesis describes the most relevant results of a single P/M technology known as Hot Isostatic Pressing applied to the processing of corrosion resistant Ni-base superalloy.

The HIP[1,2] is a pressure-assisted sintering process to fully consolidate a volume of metal powder in a body without any porosity and with outstanding mechanical properties. This result is obtained by the combination of temperature-activated diffusive solid-state mechanisms that are enhanced by the simultaneous action of a relatively high external pressure. This pressure is applied hydrostatically on the surface of the volume of metal powder, by a transmitting medium, usually high

pressurized inert gas. The volume of powder must be separated by the pressuring medium by a shell able to deform plastically as the volume of powder shrink for the densification of the powder. This shell is usually made up of an assembled mild steel capsule when the HIP temperature, usually fixed close to 0.7 of the melting temperature of the consolidating powder, is below the melting point of the steel.

A very explicative scheme of a typical HIP cycle for the consolidation of stellite powder is shown in fig. 1 adapted from [3]. The picture represents the stages of a commercial cycle: a rump-up in which the temperature and the pressure inside the chamber are raised uniformly, a dwell stage with fixed temperature and pressure and a slow cooling. A HIP cycle lasts usually several hours. The picture show also a measure of the capsule (called "can") shrinkage and three metallographies of the compacting powder at three consecutive instants of the cycle with increasing density: this picture indicates also that most of the densification occurs in the heating rump-up, while the hold-time is effective for the complete closure of residual porosity and for the effective sintering of the powder.

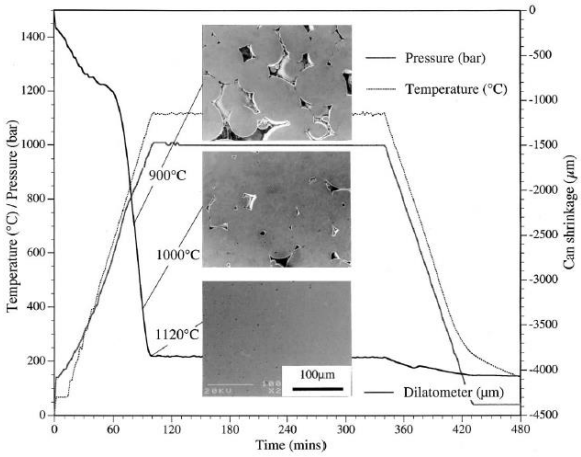

Fig 1: Scheme of a HIP cycle, adapted from Ref. [3]. Pressure and temperature are indicated in the left axis, the shrinkage of the capsule (can) on the right. Three metallographies of the sample in different compacting stages are shown.

HIP provides numerous metallurgical and technological advantages: a consolidated body is basically devoid of macroscopic defects such as porosity and macro-segregation; any material properties is essentially uniform in all the location of the part and isotropous due to the substantial hydrostatic external pressure; the gran size can be kept fine with implication in term of strength and resistance to corrosion as the case to certain stainless steel.

Finally a proper design of the capsule enables a full net-shape[4,5] manufacturing similar to casting: after the consolidation the steel capsule can be easily removed by chemical pickling. This technological solution is particularly effective when the conventional machining operations are considerably expensive and time consuming as the case for hard and strong materials like Ni-base superalloys. The advantages of this technological solution for Ni-base superalloys were discussed in detail in [6].

As discussed elsewhere, an advanced net shape engineering of the process is not an easy task. In spite of the name, the densification of a hipped part deviates appreciably from an ideal isotropic shrinkage since the final shape is modulated by the stiffness of the metal capsule, particularly effective in the early stage of the densification, when the strength of the capsule is still effective[4]. Any modeling of such a process must account for variation in volume of more than 30 % of the initial volume of powder.

This chapter introduces the physical basis of the consolidation of metal powder by hydrostatic pressure-assisted sintering, examining both the microscopic physical mechanisms responsible of the densification and a short survey of the macroscopic continuum models applied for the prediction of the densified final shape.

1.2 – Basic concepts of Hot Isostatic Pressing

The Hot Isostatic pressing of metal powders was defined as a pressure-assisted sintering technique. A sintering process consists in a thermally-activated consolidation (densification and formation of the metallic bonding between the particles) of a porous medium by microscopic mass-transport mechanisms[2], in

which the driving force of the process is given by the minimization of the surface energy $E_S=A\gamma_S$ of the pores (A is the total surface of the pores, γ_S is the specific surface energy of the material) by the pore closure. In this work only solid-state sintering processes will be illustrated. The mass-transport mechanisms during sintering are various, including volume diffusion, surface diffusion, grain-boundary diffusion, vapor transport, plastic or viscous flow; all these mechanisms will be briefly described later.

The driving force of the E_S minimization can be thought as a pressure acting in-ward on the external surface of each pore. If a crystalline porous medium of mean grain size *G* is idealized as being characterized by spherical pores of diameter *d* - a simplifying assumption representing a late sintering stage - the inherent sintering pressure can be expressed as[8]:

$$\sigma = \frac{2\gamma_{SS}}{G} + \frac{2\gamma_{SV}}{d} \qquad \text{(I.1)}$$

where γ_{SS} is the surface energy associated to grain boundaries and γ_{SV} is the solid-vapour surface energy associated to the interface of the pore between the solid and the vapor phase present inside the pore. In a final stage usually $\gamma_{SS} < \gamma_{SV}$ and $d \ll G$, so the first term of the equation (1) can be neglected and the sintering pressure is equal to the capillary force due to the pore curvature.

An actual sintering process of a porous medium like a metal powder is a much more complex process involving several stages as described in fig. 1, adapted from[1]. When metal particles are packed, the volume among them is treated as pores: in the early stage of sintering all the pores are connected, so this status is referred as open porosity. All the solid-state mass-transport mechanisms lead to the progressive formation of contacts, “necks”, among particles, disconnecting the cavities among particles (regime of closed porosity). The porosity of the medium decreases as the necks develop, determining an increase of the fraction density of the medium $D = (V_{tot} - V_{pores})/V_{tot}$, where V_{tot} indicates the volume of the whole medium. At the later stages of the process the pores tend to spherodize and are usually encapsulated inside grain boundaries.

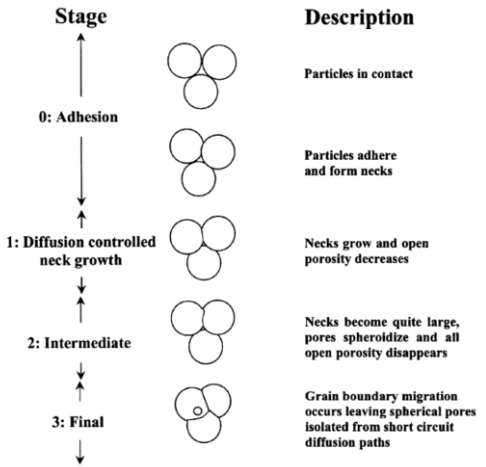

Fig 2: A sketch representing the general sintering stages in a metal powder. Adapted from Ref. from [1]

Sintering determines a densification rate that can be modelled as [7]:

$$\frac{dD}{dt} = (1 - D)Bg\frac{\gamma_{SV}}{x} \qquad \text{(I.2)}$$

where: D indicates the fractional density of the medium; B is a factor representing several physical and thermodynamical parameters of the porous system, including diffusivity, temperature and particles size; g is a geometric factor depending on how x is measured, while x indicates the dimension scale of the system (i.e. the dimension of the pores).

When external pressure is added to a sintering system, it exerts an enhancement of the densification rate that can be expressed as [7]:

$$\frac{dD}{dt} = (1 - D)Bg\left(\frac{\gamma_{SV}}{x} + P_E - P_R\right) \qquad \text{(I.3)}$$

where P_E is the effective pressure experienced at the physical contacts among particles, P_R is the residual pressure inside the pores. Due to the very small contact surface of the metal particles at the beginning of the densification, the external actual pressure P is strongly amplified in the early stage and monotonically decreases as the porosity vanishes. The effective pressure P_E at the early stage of densification was expressed by *Artz et al.*[9] for random packed spherical particles of radius *R* as:

$$P_E = \frac{4\pi R^2}{aZD} P \qquad \text{(I.4)}$$

where: a is the neck area, *Z* is the contact number per particle, *D* is the density of the system. P_E tends to P at the late stages of sintering, conventionally after density has reached more than 90%.

1.2.1 - Physical Mechanisms of densification

1.2.1.1 - *Plastic flow:*

At the initial stage of the densification, as already mentioned, P_E is high. If external pressure is sufficient, the early densification occurs by plastic yielding, even in very short time. The criterion for this mechanism is set as [10]:

$$P_E \geq 3\sigma_y \qquad \text{(I.5)}$$

The yielding continues until effective pressure reaches a limiting condition [Helle]:

$$P_{lim} = \frac{2}{3}\sigma_y ln\left(\frac{1}{1-D}\right) \qquad \text{(I.6)}$$

Real solids can experience a work hardening during a massive plastic yielding; such hardening can limit the effect of applied external pressure. The great advantages of hot pressure-assisted sintering is the thermal softening of the bulk material to consolidate. In fig. 3 typical tensile properties of the nickel-base superalloy Inconel 718 (UNS N07718) are reported [11]: the yield strength of the alloy drops from over 1100 MPa at medium-low temperature down to few tens of

MPa at 1100°C. Due to thermal softening of the material and to recovery/recrystallization processes at high temperature, the densification by plastic yielding is particularly effective for the first stage of densification and in many cases accounts for the most of the total densification.

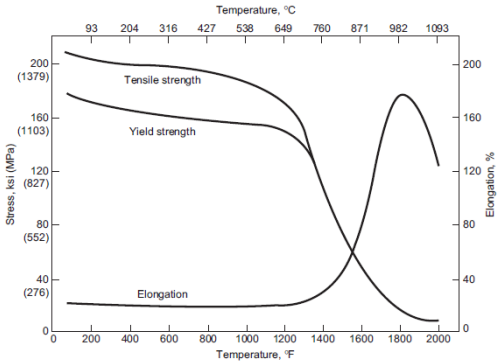

Fig 3: Tensile properties of Inconel 718 depending on temperature, adapted from Ref. [11].

1.2.1.2 - *Diffusion from interparticle boundaries*:

The contribute of diffusion from interparticle boundaries is the sum of the contribution from both surface/grain boundary diffusion and volume diffusion, through the grain boundaries and volume diffusion coefficients D_b and D_v. A representative sketch of the various diffusive contribution in sintering is shown in fig. 4, adapted from [1]. A relation was derived by Helle et al.[10] from the consideration that the rate of deposition of material on surface of particles due to the a densification rate $\dot{D}$ is equal to the rate of removal of overlapping volumes between two sintering particles (that come closer due to the sintering)[10]:

$$\dot{D} = \frac{12D^{1/3}{D_0}^{2/3}}{g(D)} \frac{Z\Omega P_{eff}}{kTR^3} (\delta D_b + \rho D_v) \qquad \text{(I.7)}$$

here D is the fractional density, g(D) is a function of the density, Ω is the atomic volume, T the absolute temperature and k is the Boltzmann constant. This expression was approximated for initial stage as:

$$\dot{D} = \frac{43(1-D_0)^2}{(D-D_0)^2}\frac{\Omega P}{kTR^3}(\delta D_b + \rho D_v) \qquad \text{(I.8)}$$

while for final stage as:

$$\dot{D} = 54 \cdot 5(1-D)^{1/2}\frac{\Omega P}{kTR^3}(\delta D_b + \rho D_v) \qquad \text{(I.9)}$$

The linear dependence of the densification rate with diffusion coefficient enlightens the strong dependence of diffusion mechanism by the temperature, since diffusion coefficient depends by temperature according to a Arrhenius behavior.

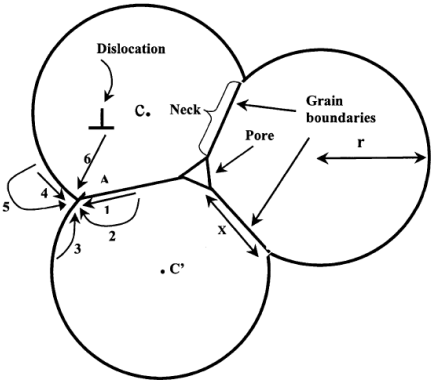

Fig. 4: A scheme of the diffusive mass-transport mechanisms contributing to densification in sintering; thress metal particles of radius *r* are sketched exhibiting the formation of necks. The picture is taken from Ref. [1]

1.2.1.3 - *Power-law creep:*

An important densification mechanism is creep[9,10]. In many systems, including the Ni-base superalloys, the involved creep behavior is described by a

power low relating the derivative of the equivalent strain of the material and the equivalent stress by a parameter *n* that represent the strain rate sensitivity[10,12]:

$$\dot{\varepsilon} = A \cdot \sigma_{eq}^{n} \qquad \text{(I.10)}$$

in which A is a parameter depending of the material and strongly by the temperature. According to [10], this power-law model leads to the following relations for the initial and the final state of the densification.

- Initial stage:

$$\dot{D} = 5.3(D^2 D_0)^{1/3} \frac{x}{R} \left(\frac{\dot{\varepsilon_0}}{\sigma_0^n}\right) \left(\frac{P_{eff}}{3}\right)^n \qquad \text{(I.11)}$$

- Final stage:

$$\dot{D} = \frac{3}{2} \left(\frac{\dot{\varepsilon_0}}{\sigma_0^n}\right) \frac{D(1-D)}{[1-(1-D)^{1/n}]^n} \left(\frac{3}{2n} P\right)^n \qquad \text{(I.12)}$$

1.2.1.4 - *Densification maps*

On the basis of the results discussed above a densification map can be drawn in order to indicate the dominant densification mechanism with a set of process parameters: Pressure P, temperature T and density D. Several examples of densification maps are described in detail in [9,10] . In fig. 5 two examples of a densification map are presented, adapted from [10]. The model describes a nickel base superalloy powder of mean diameter of 50 µm; the picture reports the relative effect of the pressure and the temperature, indicating that the power low creep is the mechanism dominant for a wide range of the relatively high pressure above 100 MPa.

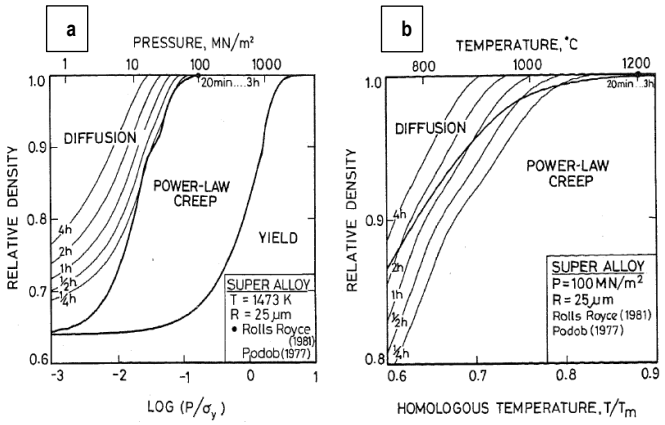

Fig. 5: HIP densification maps of a Ni-base superalloy, adapted from [10]: a) densification depending on pressure; b) densification depending on temperature. Pressure and temperature are normalized respectively over yield strength and melting temperature.

1.3 - Modelling the HIP for Net Shape manufacturing

The elaboration of modeling tools for the prediction of the HIP final shape is crucial for the effectiveness of net-shape manufacturing routes[5]. A valid prediction of the HIP shrinkage of metal parts has been successfully accomplished by the development of approximate continuum models[13-15] based on a Finite Element formulation. As discussed above, several solid-state mechanisms are involved in the consolidation process, including yielding, creep, and diffusion. The elaboration of the densification maps was used to identify the relative weight of all these phenomena on the basis of the process parameters. Most of the established continuum model approximate the densification by indivituating a single dominant mechanism, the most effective one, in particular the plastic yielding and the creep. Furthermore such models are made flexible by the introduction of phenomenological functions that improve the convergence to experimental measurements. These functions can be

related to measureable quantities and so they can be refined to adapt the model to the single case.

An interesting example a of successful simplified model is provided by the work of Ref.[4]: this model is based on a pure conium plasticity theory, supported by the consideration that most of the densification (more than 90%) occurs just in the initial stages of an HIP cycle when the external pressure in amplified by the contact among powder particles. In this case the material of the capsule is described as a perfect-rigid plastic material with the constitutive equation derived by a Von-Mises yield criterion:

$$\Phi(\sigma_{ij}) = J_2 - \tau_s^2 = 0 \qquad \text{(I.13)}$$

while the powder metal is described by the Green's plasticity criterion for porous media:

$$\Phi(\sigma_{ij}) = \frac{I_1}{f_2(\delta)} + \frac{J_2}{f_1(\delta)} - \tau_s^2 = 0 \qquad \text{(I.14)}$$

In the previous equation $\Phi(\sigma_{ij})$ represents the yield potential, I_1 and J_2 are respectively the first and the second invariant of the stress tensor of the compacted powder material, τ_s is the porous material yield flow stress, and $f_1(\delta)$ and $f_2(\delta)$ are two empirical functions depending on the fractional density of the densifying volume. The flexibility of the model is given by the possibility to adjust f_1 and f_2 in order to better approximate the shrinkage of the compact.

The most popular model of macroscopic shrinkage, known as the Abouaf model [13,14], is an evolution of the Green model for porous media, and it is based on the assumption that the densification can be essentially described as power-law creep process. The constitutive equations are then derived from a creep potential of the form [13]:

$$\Omega = \frac{A}{n+1}{\sigma_{eq}}^{n+1} \qquad \text{(I.15)}$$

With σ_{eq} Von-Mises equivalent stress, A is a parameter depending on activation energy and on temperature, *n* is reciprocal of the strain rate sensitivity. In this case the equivalent stress can be expressed as the sum of a hydrostatic contribute and a deviatoric term according to the relation:

$$\sigma_{eq}^2 = f(\delta)I_1 + 3c(\delta)J_2 \qquad \text{(I.16)}$$

where $f(\delta)$ and $c(\delta)$ are two empirical phenomenological function, depending on the density δ of the powder, whose use is similar to the previous f_1 and f_2.

$f(\delta)$ and $c(\delta)$, as well as $f_1(\delta)$ and $f_2(\delta)$, can be related to measurable quantities and then derived. An example of such procedure is mentioned in Ref. [15]. It can be demonstrated that in a uniaxial compression test the stress measured on a compact material ($P_z(\delta = 1)$) and on the porous medium ($P_z(\delta < 1)$) at the same strain rate can be related by the relation [13]:

$$\left|\frac{P_z(\delta=1)}{P_z(\delta<1)}\right| = (f + c)^{\frac{n+1}{2n}} \qquad \text{(I.17)}$$

The relative intensity of *f* and *c* are the determined by another set of experiments relating *f* and *c* to the densification rate $\dot{\delta}$ in typical conditions. For example in a condition of hydrostatic pressing by a pressure P, $f(\delta)$ is given by:

$$f(\delta) = \frac{1}{9}\left(\frac{\frac{\dot{\delta}}{\delta}}{A \cdot P^n}\right)^{\frac{n+1}{2n}} \qquad \text{(I.18)}$$

The empirical refining of these functions is anyway a complex task since it requires in a certain sense the simultaneous knowledge of the temperature, the porosity and the densification rate of a representative HIP cycle, instant by instant.

1.4 - Effectiveness of the solid-state bonding.

The complete densification of a HIP process is just one aspect of the most general consolidation process occurring during HIP. The mechanical properties of

the consolidated material will depend crucially also by the quality of the solid-state bonding among the particles [7]. The bonding is strongly affected by the surface structure and chemistry of the powder particle, in particular by the presence of thin layers of oxides that can retard or prevent the bonding [16,17], i.e. basically acting as diffusion barrier. This aspect will be discussed in detail in the chapter IV in which the mechanical properties of the Ni-base alloy are discussed.

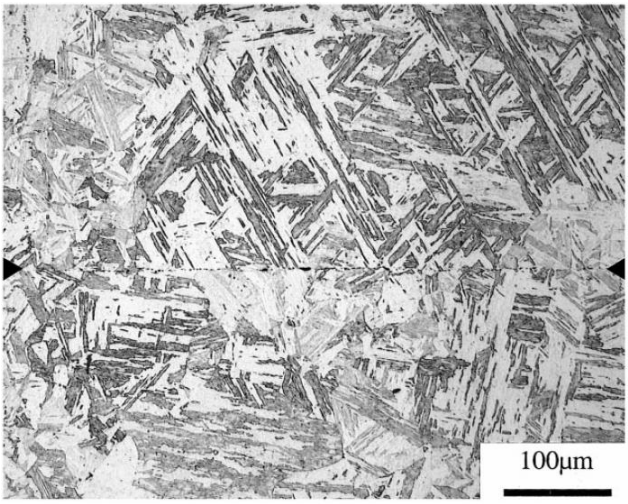

Fig. 6: Metallography of a solid-state diffusion bonding interface in a 17-4 PH Stainless steel. The interface (indicated by two black arrows on both sides of the picture) is characterized by the formation of a layer of oxides. Picture adapted from Ref. [3].

A HIPped material can be fully dense but intrinsically weakly bonded with very bad mechanical properties. In order to conclude this brief overview of the main concepts of HIP an analogy is suggested with the very similar process of solid-state diffusion bonding [18,19] to show the typical issues of a diffusion bond. A demonstration of weak diffusion-bonded interface in shown in fig. 6 adapted from Ref. [3]: the bonding interface (indicated by two black triangles at the sides) between two bodies of stainless steel is characterized by the dense precipitation of oxides during the dwell time degrading the quality of the bond. A substantial improvement

can be reach changing the atmosphere of the process or the roughness of the surface.

The diffusion bonding can be heavy impacted when the surface oxide are very stable, like in the case of the aluminum oxides [20]. An interesting overview of the possible strategies to overcome this limitation is presented in Ref. [20]. Here two picture are adapted in fig. 7 from this cited reference with two mechanical ways to break the oxide and promoting the bonding: fig. 7 a) a heavy mechanical deformation that breaks the oxide since they are less ductile than the substrate and (fig. 7 b) the effect of the surface asperities obtained by a proper grade of roughness.

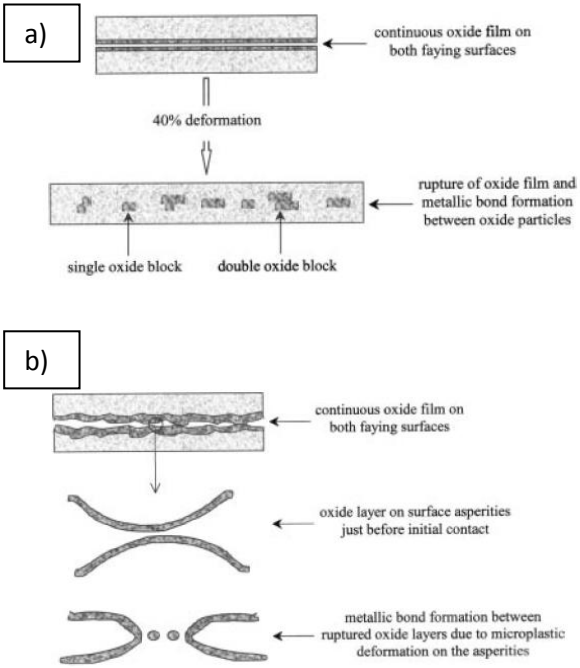

Fig 7: Behaviour of the oxide surface layer in solid-state diffusion bonding of two interfaces of aluminum: a) oxide breaking by heavy plastic deformation; b) surface oxide breaking by surface roughness. Picures adapted from Ref. [20].

Chapter II

Scope of work and experimental method

2.1 - *Selection of material and scope of work*

The research activity concerns the metallurgical and mechanical investigation of the corrosion resistant Ni-base superalloy N07626 fabricated by HIP [21]. The N07626 is a very promising alloy for application in critical parts in Oil & Gas turbomachineries exposed to very aggressive gas environments, rich of chlorides and sulfides. The N07626 alloy exhibits mechanical properties similar to the widely used Inconel 718 (N07718) but with outstanding resistance to corrosion. A detailed description of the benefits resulting from the introduction of the P/M HIP technology for the manufacturing of this Ni-base is provided in [6].

Since most of the activity was conducted in collaboration with the Materials and Processes Engineering Department of GE Oil & Gas any sensitive proprietary information has been removed. In order to facilitate the analysis of the work all results are presented in normalized unities.

The scope of the activity can be condensed in the points below:

i. Identify the effect of the cycle parameters in the densification process of the pressure-assisted sintering for the Ni-base alloy N07626, in particular the effect of pressure and temperature;
ii. Assess the reliability and the stability of the material properties resulting from a standardized production cycle, including the powder consolidation and a post-consolidation quality heat treatment;
iii. Investigate the peculiar metallurgical aspects of the resulting novel material that are intrinsically related to the powder-based nature of the processing method, and discuss their impact in term of design requirements;

iv. Investigate the effect of varying the process parameter on the mechanical properties of the material in order to identify perspectives of future improvements.

2.2 - Experimental procedure

2.2.1 – Analysis of the densification: lab scale fast sintering by Spark Plasma Sintering

Due to the limited accessibity to HIP facilities, the study of the influence of the process factors (Pressure and Temperature) on the physical mechanisms of the densification of N07626 powder was conducted on a small scale system by setting a uniaxial hot pressing condition for the metal powder. These experiments were conducted by a fast and effective pressure asisssisted method known as Spark Plasma Sintering [22-26]. The specificity of this process consists in the unique method of heating the metal powder by a flux of electric current flowing through the mold of the powder and the metal powder itself. If the metal powder is a good conductor the sintering is associated to novel solid-state phenomena.

In the case of Ni-alloy N07626 it will be shown in the following that the intrinsic contribute of the current flow through the powder can be neglected. So the densification process is considered as a simple uniaxial assisted sintering process. Although the uniaxial loading geometry leads to differences in the mechanics of compaction compared to hydrostatic pressing, the global effect of the the variation of pressure and temperature can be clearly appreciated and gives information for the understanding of a full scale HIP compaction.

Sintering was performed by SPS-1050 machine (Sumitomo Coal & Mining Co. Ltd). The powder was poured in a graphite die with a cylindrical cavity of 10 mm of diameter, closed on the bottom and pressed by a conductive punch on the top. The punch supplies electrical current to the system (die + powder) by means of pulsed DC voltage (pulse cycle: 12 pulses ON/2 pulses OFF, duration 3 ms) and at the same time exerts pressure on the powder. The temperature of the die was measured by a pyrometer and the temperature inside the cavity is extrapolated by means of a system calibration.

The sintering cycles were conducted in conditions of moderate vacuum (6-8 Pa) to assist the degassing of the powder during densification. The samples produced were cylinders of 10 mm of diameter and 6 mm of height.

The effect of pressure and temperature was investigated by considering 6 conditions: a fixed relatively-low pressure with three temperature conditions, and a fixed relatively-high temperature with three pressures. All the condition are listed in the tab. 1

Furthermore the effect of current flow in the densification was investigated by comparing a group of repetition of cycles with a special cycle in which the powder was insulated electrically by the graphite dye.

Sample name	Electrical insulation	Temperature	Pressure
Sps1	No	T max	25 MPa
Sps2	No	0.92 T max	25 MPa
Sps3	No	0.83 T max	25 MPa
Sps4	No	0.96 T max	63 MPa
Sps5	No	0.96 T max	50 MPa
Sps6	No	0.96 T max	38 MPa
spsS	No	0.96 T max	60 MPa
spsI	Yes	0.96 T max	60 MPa

Tab 1: List of cycle parameters applied in SPS experiments.

2.2.2 - HIP process and parameter

This research activity reports the metallurgical and mechanical investigation carried out on several consolidated parts made by HIP of pre-alloyed metal powder, applying both a standard proprietary processing procedure and different experimental processing conditions. All HIP processing involved the following stages:

1. assembly of the capsule, referred also as “can”: the capsules parts were fabricated by mild steel and welded.

2. filling of the can by the metal powder, applying a continuous vibration of the capsule in order to densify the powder as much as possible;
3. out-gassing of the filled can by vacuum pumps and sealing of the filling apertures.
4. Consolidation in the HIP furnace;
5. Quality heat treatment, consisting in a solution treatment and an aging;

All stages 1-4 were performed by two external suppliers, that will be called supplier 1 (S1) and supplier 2 (S2). The details regarding points 1-3 are suppliers proprietary and were not disclosed. In the following it is assumed for these stages that the variability within suppliers is small and can be considered as the intrinsic variability of a HIP processing.

The stage 4 was done by the suppliers applying a GE defined set of cycle parameters including the 1) HIP dwell temperature; 2) the external gas pressure; the cycle time; the heating and pressurizing rump-up are proprietary details of suppliers. Such a standard set of parameters will be referred as ST-HIP for both suppliers: the possible differences in the heating/pressurizing rump-up are neglected. The ST-HIP was previously optimized to reach full density. Three further sets of experimental parameters were considered in the investigation: a dwell temperature increased by +7% with the ST-HIP pressure (T2-P1-HIP); the ST-HIP temperature and a dwell pressure increased by +25% (T1-P2-HIP); and an increase of both dwell HIP temperature and dwell pressure (T2-P2-HIP). The HIP dwell temperature and pressure are important factors in the kinetic of the densification process and affect the solid-state transformation and the mechanical deformation mechanisms of the metal powder particles, respectively. Since the ST-HIP cycle was already optimized for full densification, the further parameters were selected in order to investigate the latter aspects, in particular:

- the increased HIP temperature was selected to study the impact on grain growth and on solid-state transformation of the precipitates formed during HIP cycle;

- an increased pressure was considered for possible effect for a more efficient fragmentation of the surface oxides of metal powders. Furthermore, since grain growth is a very temperature-sensitive mechanism, a limited temperature increase

was chosen in order to prevent a massive growth and an excessive softening of the material.

The stage 5 was carried out by supplier S1 and S2 and in the GE MPE Laboratories: two heat treatments were considered: a standard proprietary heat treatment (ST-HT) consisting in a solution annealing followed by a precipitation-hardening aging and an experimental cycle (HT2) with the solution temperature increased by about 4% and the aging kept fixed; the experimental solution temperature was equal to experimental T2 HIP temperature.

2.2.3 - Powder

In the aim to characterize the sensitivity of the HIP process to the raw material properties, i.e. the properties of the metal powder, the investigated parts were made by pre-alloyed metal powder supplied by 4 different producers: p1, p2, p3 and p4. The exact chemical composition of each powder type was selected to be compliant with the Oil & Gas NACE Standards for the alloy N07626. A nominal composition of the alloy N07626 compared with the Inconel 718 is reported in tab. 2.

	Nominal composition (weight %)							
Alloy	Ni	Cr	Mo	Nb	Al	Ti	Cu	Fe
N07718	53.5	18.2	3	5	0.5	1	Trace	Bal
N07626	Bal	21.5	9	5	0.6	0.6	Trace	max 6

Tab 2: Nominal chemical composition of the alloy N07626 and the alloy N07718 (Inconel /18)

The powder p1, p2 and p3 were produced by inert gas atomization, using argon as atomizing medium; the powder p4 was instead produced by plasma atomization of a pre-alloyed metal wire. The maximum size of the metal powder was set with particle diameters ≤ 150 μm; for powder p1 and p4, two further experimental lots of metal powder sieved ≤ 50 μm were procured. The powder p1-p3 presented very small deviations in the alloying elements and the size distribution is similar due to a similar standard atomizing technique: in the following they are assumed to be equivalent regarding alloy elements composition and size distribution, but not

regarding the content of the trace elements C, S, O, N, that determines the surface properties of metal particles. The powder p4 was treated as not equivalent for the very different processing method.

The reason for the use of several distinct powder varieties is described in the following. An important aspect to clarify in this investigation is the intrinsic variability of the process using a single standard set of processing parameters (HIP + HT); this task is achieved by using equivalent raw material (small deviation in chemical composition included the content of trace elements). As will be discussed in the rest of the chapter, the accumulation of interstitials elements, in particular oxygen has a crucial role in controlling the ductility and the toughness of the material. The variation of this property for experimental purpose is intrinsically difficult when metal powder is produced by a single supplier according standard industrial practices. So in the following the samples obtained with powder p1 or p2 are considered as a reference material, while the lots of powder p3 and p4 were introduced in order to represent increasingly degraded properties of the same material with the enhanced accumulation of interstitials, in particular the p4 powder represents a worst case. The normalized oxygen content measured on representative lots of the four different powder with the same maximum particles' size is reported in the tab 3 .

Powder type	Normalized Oxygen concentration
P1 (reference)	1
P2	1.2
P3	2.4
P4	2.2

Tab 3: Normalized oxygen concentration in the metal powders used. P1 powder is the reference.

The experimental processing parameters discussed above were tested on the standard powder p1 and on the degraded powder p4 in the aim of investigating the sensitivity of the material properties to different processing conditions. A complete summary of all experimental condition is presented in tab. 3.

List of HIP processing conditions				
Processing identity	HIP condition	HT condition	powder	Powder size
T1-HT1	standard	Standard Sol. + aging	P1	d ≤ 150 µm d ≤ 50 µm
			P2	d ≤ 150 µm
			P3	d ≤ 150 µm
			P4	d ≤ 150 µm d ≤ 50 µm
T2-HT1	T + 7%, same pressure	Standard Sol. + aging	P1	d ≤ 150 µm d ≤ 50 µm
			P4	d ≤ 150 µm d ≤ 50 µm
T1-HT2	Standard	Solution temperature +5%, same aging	P1	d ≤ 150 µm d ≤ 50 µm
			P4	d ≤ 150 µm d ≤ 50 µm
T2-HT2	T + 7%, same pressure	Solution temperature +5%, same aging	P1	d ≤ 150 µm d ≤ 50 µm
			P4	d ≤ 150 µm d ≤ 50 µm
Pr2-HT1	Pressure +25%, same temperatu re	standard	P1	d ≤ 150 µm d ≤ 50 µm
			P4	d ≤ 150 µm d ≤ 50 µm

Tab 4: List of applied HIP and heat treatment parameters with the metal powders used.

2.2.4 - Mechanical testing

Numerous mechanical tests were conducted on parts produced both by standard and experimental process conditions. A large part of such experiments concerned medium-large thick pieces with diameters bigger that 100 mm and height bigger that 150 mm, that were produced by S1 and S2 along several years according to proprietary ST-HIP process conditions. The samples for tests were cut in the core of the samples and close to the steel capsule in portions of the material that were found to be prone to the accumulation of interstitial elements. Such zones usually extend inward for few tens of mm from the external capsule. These volumes are referred in the following as Oxygen Affected Zones (OAZs).

Since the mechanical tests were conducted in part in the laboratories of GE Oil & Gas and in part by external certified labs, all tests were conducted according to international ASTM standards.

2.2.4.1 - Tensile testing

The tensile testing was conducted in the GE Lab and by external testing laboratories (ExL) according to the ASTM standard E8. In all tests cylindrical sample were used as shown in fig 1 adapted by the ASTM E8 document [27].

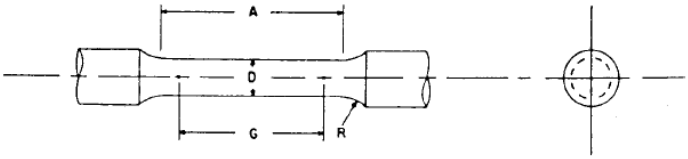

Fig 1: Sketch of the tensile specimens drawing specifications, adapted from Ref.[27].

2.2.4.2 - Impact toughness

Charpy V-Notch (CVN) tests were performed both in GE Lab and in external certified laboratories according to ASTM E23 standard. The type of specimen used is shown fig 2 adapted from the ASTM E23 document [28]. Furthermore on samples produced by experimental conditions the CVN tests were performed by an instrumented Charpy pendulum with 300J of maximum available energy at the

Department of Industrial Engineering of the University of Trento. An instrumented Charpy pendulum is able to record the curve of the experienced load by the head of the pendulum over the deflection of the detector. This curve gives relevant information of the modulation of the energy absorption during the impact, so describing also the fracture behavior of the specimen. A valid description of the interpretation of results is provided int the ASTM E2298 document.

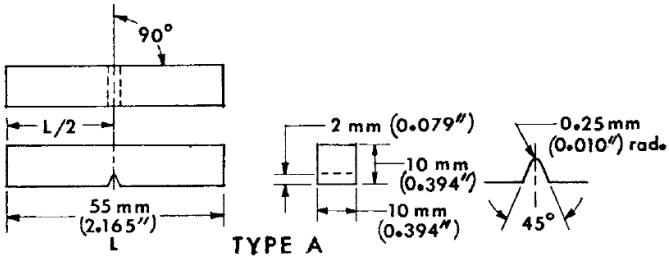

Fig 2: Sketch of drawing specifications for Charpy V-Notch specimens, adapted from Ref. [28].

2.2.4.3 - Fracture toughness

The fracture toughness J_{IC} of the samples was measures by an external certified laboratory according the ASTM E1820 standards. This method consists in the determination of a critical stress intensity parameter (J_C) by the loading of a precracked specimen [29]. In this investigation, compact specimens were used with dimensions compliant to the specification of the standard inllustrated in fig 3, adapted from the ASTM E647 document [30]. The fracture toughness is determinated by the calculation of a resistance curve of a quantity J (a line integral derived by measurable quantities described in the standard) over the length of the quasi-static propagating crack. If the condition of plain strain is achieved by the geometry of sample, a critical value of J can be defined that individuates the onset of fracture instability. The value of J_{IC} corresponds to the vaule of J of the J-R curve at the offset of 0.2 mm of crack length if other requirements are fulfilled. In some sample no stable crack propagation was reached; in these cases the measured value of J at the 0.2 mm is used as indicative value of fracture toughness.

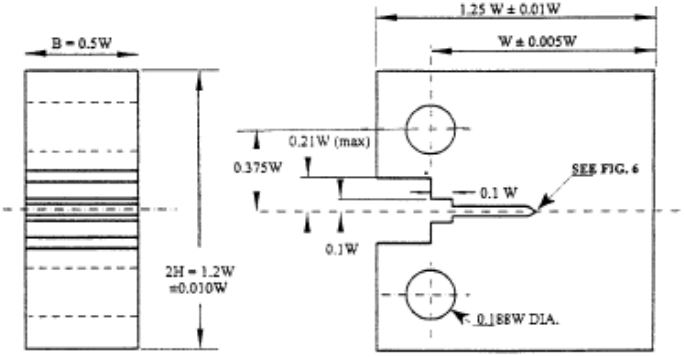

Fig. 3: Sketch of drawing specifications for Compact Specimens for J_{IC} fracture toughness test, adapted from Ref. [30].

2.2.4.4 - Fatigue crack propagation rate

The propagation of a fatigue crack was measured according to ASTM standard E647 on a pre-cracked CT specimen by an ExL. This method consists in the determination of a crack propatation rate, expressed as the increment of crack length *Δa* over the number of fatigue cycle *N*, depending on a stress intensity range $\Delta K = K_{max} - K_{min}$. The crack advance is determinated on a pre-cracked compact specimen as what illustrated in fig 4 adapted from the ASTM E647 document [31]. In the tests reported in this work, a value of 0.1 was imposed to the ratio K_{min}/K_{max}.

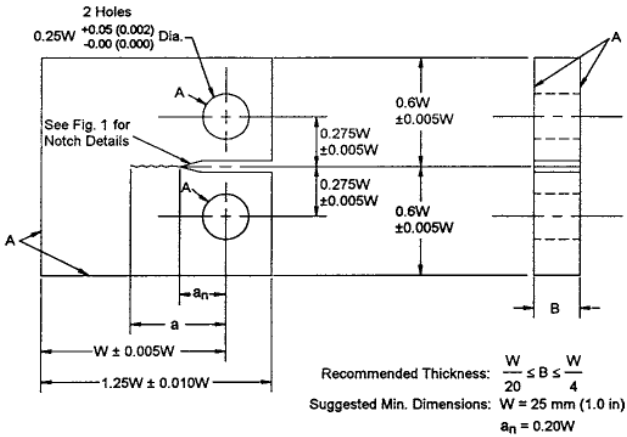

Fig 4: Sketch of drawing specifications for Compact Specimen for Fatigue Crack Growth Rate test, adapted from Ref. [31].

2.2.5 Metallographic analysis

2.2.5.1 - Optical metallography and sample preparation

The metallographic analysis of the samples was performed in the GE Laboratory by optical microscopy and by Scanning electron Microscopy (SEM). The metallographic specimens were prepared by applying a series of lapping steps by grinding paper and a final polishing by clothes using a first step by 3 µm diamond paste for 5 min and a last polishing stem by a nanometric silica suspension (OPS) for 10 minutes. Where applicable an electrochemical metallographic etching was conducted using a 80% H_3PO_4 + 20% H_2O solution with voltage = 4.5 V and hold time fo 5-10 s.

2.2.5.2 - Electron microscopy

The electron microscope used was a Field-Fmission Gun (FEG) Zeiss SUPRA 50 equipped with an Oxford X-Ray detector for Energy Dispersed Spectroscopy (EDS) microanalysis and an Oxford Electron Backscatter Diffraction (EBSD) detector. The EDS and the EBSD analyses were conducted by the Oxford Suite Aztec and the elaboration of the EBSD data was further completed by the Channel 5 suite Tango.

The EBSD [32] is based on the identification of the local crystalline structure of a point on a metallic surface by the analysis of characteristic diffraction pattern produced by the interaction of the electron beam with the crystalline structure of the metal. These diffraction patterns are produced as electrons backscattered by a small spot on the surface of the specimen where the electron beam is converged in a single spot. The pattern are detected by a CCD detector. A detailed overview of the technique can be found in Ref. [33]. By the use of a FEG SEM the resolution of an EBSD analysis can reach values lower than 100 nm. If a surface is sampled in a grid of points a map of crystallographic orientations is obtained. In this work the EBSD was used in particular for the analysis of the grains and of grain boundaries.

The grain analysis was performed by imposing a misorientation of 10° across GBs to identify distinct grains. Areas of 1 mm^2 were scanned by EBSD with a step smaller than 2.25 μm. A comparison of the identified area with total area indicates that more than 95% of the scanned area is reconstructed. Due to the large occurrence of twins found in the materials analyzed, a tight criterion of exclusion for special boundaries of 60° of misorientation with axis of the {111} crystallographic direction was imposed: a narrow tolerance of 2° around 60° was selected. Although this criterion is certainly not exhaustive, it allows identifying most of the grains.

2.2.5.3 - Chemical analysis of the composition

In the portion of materials where the samples for mechanical tests were cut, a chemical analysis of the content of traces elements was conducted by external testing Labs. The reference standard was individuated in the ASTM standard E1019.

Chapter III

Pressure assisted sintering of the Ni-base alloy N07626

Part of this chapter has been published in Ref. [34]

3.1 - Short introduction to Spark Plasma Sintering

This paragraph is intended as providing just a very basic introduction of the Spark Plasma Sintering (SPS) technique in order to understand the meaning of the experimental results. A very detailed introduction can be found in. Ref. [22-26]. The SPS is a recently introduced sintering technique based on the concurrent application of pressure and heat through a current flow through the powder to be consolidated. The current flow is the specificity that distinguishes the SPS from other conventional hot pressing techniques, like uniaxial hot pressing or Hot Isostatic Pressing. Then SPS combines the pressure-assistance of other conventional methods with a fast current heating, allowing powders to reach very high sintering rates: a few minutes even to sinter to full density for most metals and alloys, limiting severely the grain growth and opening many perspectives about fine-structured materials. The effect of current flow is today still not well understood, and this fact explains the increasing attention of the international community about the topic. The current heating is very fast and many works suggest it can affect only a narrow layer on the surface of the powder particles, inducing a localized overheating while keeping temperature lower inside the particles [35]. Many researches have tried to investigate the possibility of electric sparks among neighboring particles (this phenomenon gives the name) [36]. In any case today it is crucial to clarify the effect of current flow on diffusive phenomena and subsequently on the intrinsic behavior of the sintering process.

3.2 – SPS of the Ni-base alloy N07626

3.3.1 - SPS cycle:

The experimental SPS cycles were conducted according to a scheme sketched in fig 1. It can be divided in six main stages (A-F) that are listed in tab III.1

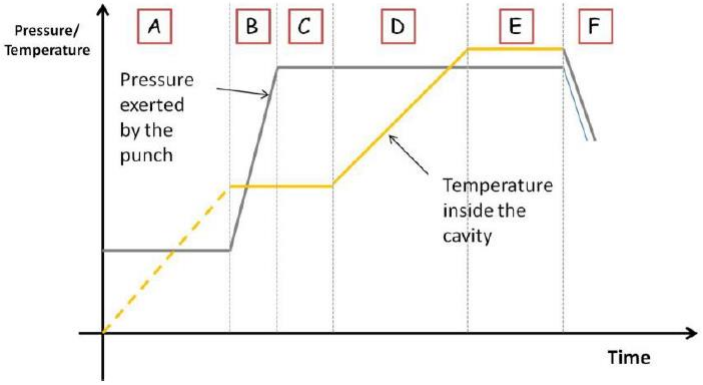

Fig 1: Scheme of the SPS cycle applied with the division in stages listed in tab. 1. The picture was published in Ref. [34].

Stage	Pressure	Temperature	Duration
A	Holding at 19 MPa	Heating from room temperature to 0.5 T_{max}	3 min
B	Constant increase of pressure to 25,5 MPa	Holding at 0.5 T_{max}	1 min
C	Holding at 25,5 MPa	Holding at 0.5 T_{max}	1 min
D	Holding at 25,5 MPa	Constant heating to maximum temperature	6 min
E	Holding at 25,5 MPa	Holding at maximum temperature	4 min
F	Removing of pressure	Free cooling	

Tab 1: SPS stages with applied parameters of temperature, pressure and time.

3.2.2 - Effect of temperature:

In fig. 2a the punch displacement-rate over time is shown for the samples sps1, sps2 and sps3. In the fig. 2 and in the following only the stages C to F are considered. The fig. 2b shows the temperature values detected by the pyrometer over time: it is worth to note that the samples reach three distinct temperatures in the same time interval, meaning three distinct increasing heating rates. The displacement-rate curves indicate that the densification starts at the same time *t* for the three samples, the densification rate increases monotonically to a maximum, followed by a fast decrease; the slope of the curves increases for higher dwell temperature. For the sample sps3 the maximum is reached inside the stage D, i.e. during constant heating, the rate decrease starts in the stage D as well and continues through the stage E of isothermal holding to zero, indicating the stop of the densification. For the samples sps1 and sps2 the maximum of the densification rate coincides with the end of the heating stage D and is followed by a fast decrease that does not reach the zero, indicating that a slow densification persists during isothermal stage E.

In fig. 3 the optical micrographs of the samples sps1,sps2 and sps3 are shown. In samples sps1 and sps2 a very high porosity is observed, while sps3 is almost full dense: the image analysis indicates approximately 30% of porosity for sps1 and 18% for sps2, while the value is much lower for sps3 (about 2%). It is worth of noting that the powder particles (mostly the bigger particles), still clearly discernible in sps1 and sps2, appear to retain their spherical shape almost unchanged, indicating that the pressure applied of 25.5 MPa is not sufficient to plastically deform the particles to a massive extent even above the relatively high temperature of 0.92 Tmax (sps2). Sintering is evident with the increasing formation of necks from sps1 and sps2 and the disappearing of any prior-particles structure in sample sps3.

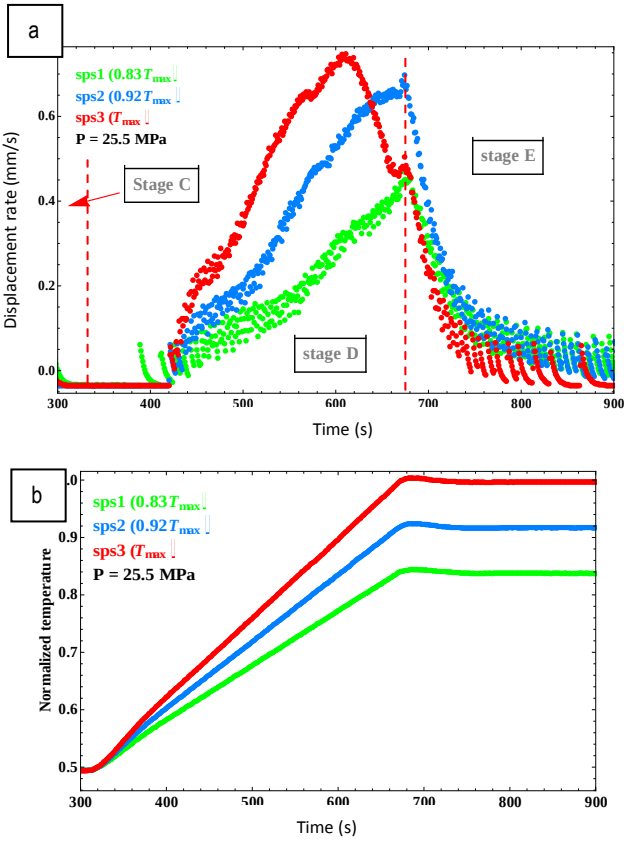

Fig 2: a) densification rate as function of time for the densification cycle of samples sps1, sps2 and sps3; b) temperature profile in the cycle for the same samples.The picture was published in Ref.[34].

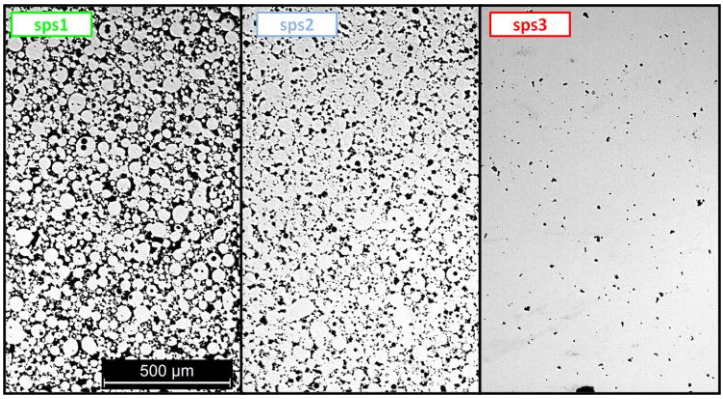

Fig 3: Optical metallography of samples sps1, sps2 and sps3 showing increasing final density. Picture published in Ref. [34].

3.2.3 - Effect of pressure

The effect of pressure on the densification rate of N07626 powder was investigated by varying the compacting pressure at constant maximum temperature. The behaviour of the densification rate over time of the samples *sps4*, *sps5* and *sps6* is presented in fig 4 The picture confirms that the increase in pressure produces a small increase of densification rate of the order of few percents. This effect is not so marked as it was found regarding the temperature. The increase in pressure lead then to a slightly faster densification.

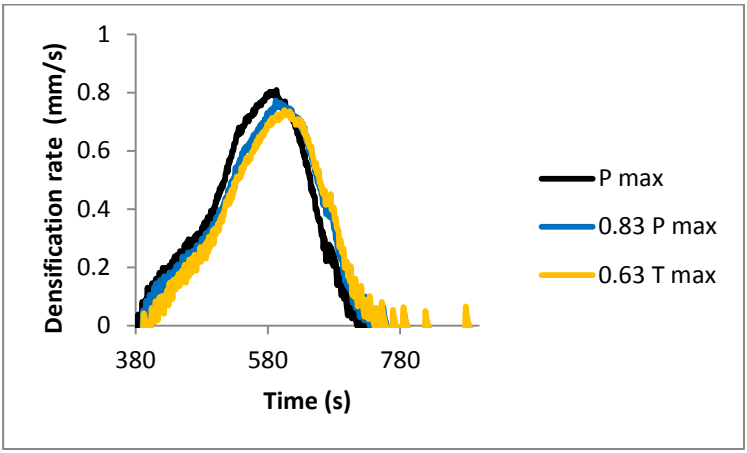

Fig 4. Densification rate as function of time for samples sps4, sps5 and sps6: the densification was conducted with the same temperature profile and three different maximum pressures.

3.2.4 - Effect of electric current

As anticipated the effect of current flow in the densification process of the N07626 powder was investigated in order to identify possible significant deviation from a pure hot pressing. For this scope several tests were repeated with the same process conditions keeping conductive the powder in order to get a significative statistic of the densification rate of the powder in a baseline set of parameters (cyle *spsS*). The same cycle was then repeated after isolating the powder from the current (cycle *spsI*) . The result is shown in fig. 5 in which the densification rate of all these sample is compared. The picture indicates that the effect is very small, appearing with a miminal rigid shift of the densification curves toward higher current value. In any case the shape and the intensity of the curve is not impacted. This fact suggest that with Ni-alloys the SPS can occur mostly by simple Joule effect heating.

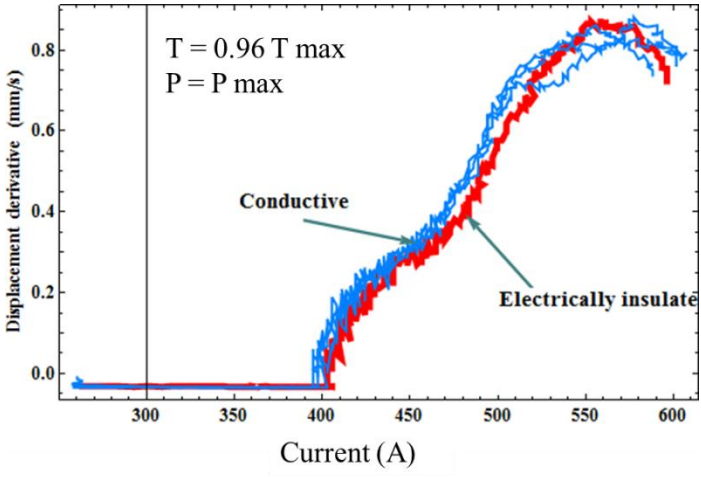

Fig. 5: Densification rate as function of the measure current flow of a group of reference samples processed according to cycle spsS (blue lines) compared with the densification rate of spsI sample (red line).

3.3 - Extension of SPS result to a full-scale HIP

The investigation of the SPS of powder of the N07626 alloy demonstrated that in a pressure-assisted sintering condition, with temperature and pressures comparable with a real HIP process, the variation of the pressure has a limited impact in the densification rate of the system. On the other hand the effect of a decrease of temperature of just less than 8% from Tmx strongly modifies the densification curve and produces samples with a significant porosity.

Scaling these result on a HIP process, it follows that the densification rate in the initial stage with high porosity will be driven mostly by variation temperature. This result suggest than the densification behavior for N07626 powder could be dominated by diffusive mechanism (creep and diffusion) that are characterized by a strong dependence on temperature. The role of the plastic yielding instead is considered less important. Comparing this interpretation with the work of Ref. [14], the collected data suggest that the densification of N07626 and similar alloys is dominated by creep.

A higher HIP temperature will lead to a faster densification. In this phase the pressure has a mush smaller impact. So the intensification of the pressure is not expected to impact the cycle time.

Chapter IV

Microstructure and mechanical properties of the P/M alloy N07626

Part of this chapter has been submitted for publication [37]***:***

This chapter presents the results of the analysis of the microstructure and of the mechanical properties of the P/M alloy N07626 produced by Hot Isostatic pressing. The chapter introduces the metallurgy of the alloy and describes the representative microstructure of a standardized material, processed according defined set of parameters (ST-HIP), and including also the analysis of several experimental set of parameters. The metal powder used was mostly p1, representing the reference, and the powder p3 and p4 as case studies. The mechanical properties are measured at room temperature and they include tensile properties, impact toughness, fracture toughness and the crack propagation in condition of fatigue. In the final section of the chapter the effect of the variation of HIP process parameter is presented in order to illustrate possible perspectives of improvements.

4.1 – Metallurgy and microstructure

4.1.1 - Metallurgy of N07626 and similar Ni-base alloys

The physical metallurgy of N07626 is discussed in tight analogy with the two well-known Ni-base superalloy Inconel 718 (N07718)[21,38-40], widely used in gas-turbine components, and the corrosion-resistant alloy Inconel 625 (N06625)[41,42]. Actually N07626 was introduced as a possible replacement of IN718 for applications requiring comparable strength and more resistance to corrosive environment [21].

The microstructure of the IN718 is characterized by a fcc austenitic matrix (γ phase) that is strengthen by solid-solution of heavy elements and by the precipitation-hardening of several phases as well documented in Ref. [11]. The major contribution of strengthening is attributed to the Ni_3Nb γ", a metastable phase that tends to be replaced by the Ni_3Nb δ phase in condition of averaging. The occurrence of δ phase, precipitating preferentially at GBs as thin platelets, is considered detrimental for mechanical properties, in particular for creep resistance. The low concentration of Al and Ti in IN718 is associated to a minor contribution to the strengthening by the Ni_3Al,Ti γ' phase; in N07626 the fraction of Al and Ti is lower than IN718, so the contribution of γ' is considered negligible. The Inconel 718, the Inconel 625 and the N07626 contain elements that are strong carbide former (Nb and Ti): several species of carbides were actually reported in Ni-alloys, depending of the heat treatment conditions. The typical microstructure of the precipitated γ"+ γ' phases for an as-HIP powder metallurgy Inconel 718 was studied in Ref. [39] through transmission electron microscopy: the precipitates appear as ordered elongated disk-shaped platelet of dimensions ranging from a few nm to a few tens of nm. An example of these precipitates can be observed in the fig.1 where the cited TEM image is shown; in the same material Ref. [39] reported a very representative microstructure of a GB that is the preferential site for the precipitation of δ phase and MC carbides. The structure of the γ"+ γ' in the investigated N0726 is assumed to be very similar to what described in Inconel 718.

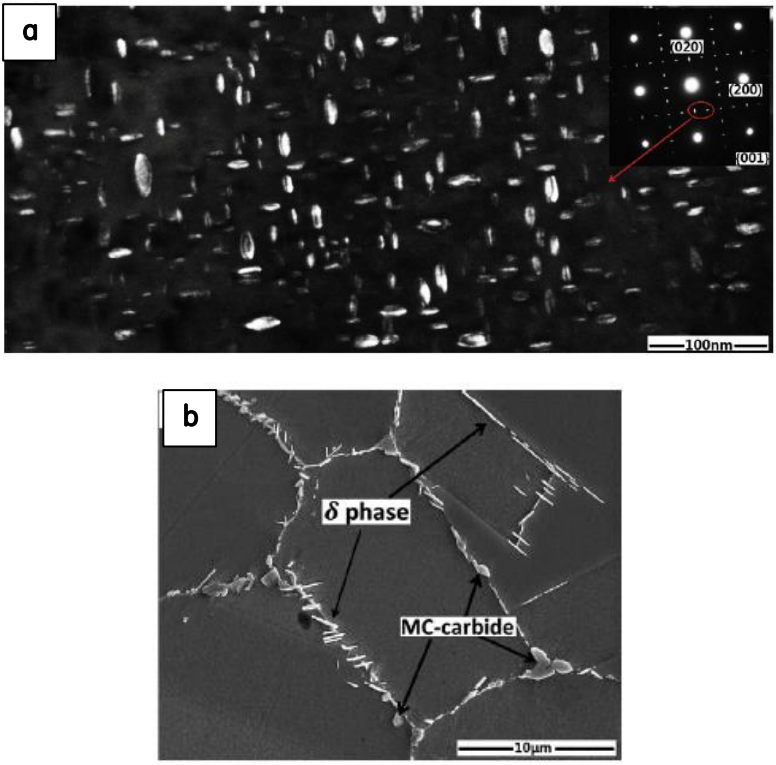

Fig 1: a) Transmission Electron Microscopy image of the precipitated γ"+ γ' phases in an PM as-HIP sample of Inconel 718; b) SEM image of the precipitated δ phase and carbides at the grain boundaries in the same sample of (a). Both pictures are adapted from Ref. [39].

The occurrence and the thermodynamic stability of the phases present in an idealized alloy N07626 can be described by a thermodynamic simulation obtained by the software Thermocalc using the material database TTNI8. The mass fraction of all stable phases occurring in the range of temperature 225°C-1220°C is presented in fig. 2: these results were based on a chemical composition representative of reference material. The indicative ranges of temperature of the HIP, solution annealing and aging treatment are also indicated in the figure. In the temperature range of HIP and solution annealing the simulation predicts the dissolution of the hardening phases (γ',γ" and δ). The small oxygen concentration leads to the

formation of corundum-like stable M_2O_3 (M = metal) phase (mostly alumina) that is retained all along the temperature considered. The software predicts also the formation of a small fraction of a fcc phase distinct from matrix, called FCC_#2. The analysis of composition of the FCC_#2 (not shown here) indicates that it is based on Nb and C, with residual content of Mo, so it is identified as MC Carbide. The thermal stability of NbC is described in Ref. [43] for Inconel 718, where the solvus temperature is found at 1267°C. In the range of temperature of the aging treatment the stable phases are the γ matrix and the phases γ' and δ. The hardening phase γ" (Ni_3Nb) is absent since it is actually metastable and tends to transform to the stable δ in a prolonged aging. The γ' phase is present in small quantities due to the small concentration of forming elements Al and Ti; so its role in hardening is secondary. At the aging temperature the $M_{23}C_6$ type carbide is stable, so even the precipitation of secondary carbide is expected, as the investigation of Inconel 625 in Ref. [42] confirms. In the latter the precipitation occurs preferentially along GBs.

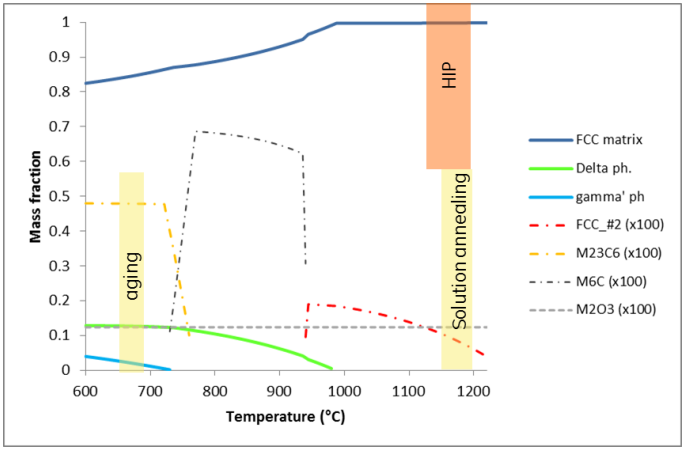

Fig 2: Simulation of phase amount at the thermodynamical elequilibrium as function of temperature for a representative chemical composition of N07626 alloy. The temperature ranges of HIP and heat treatment adopted in the investigation are also indicated.

4.1.2 – Microstructure of HIP N07626 samples

The microstructure of HIPped N07626 is characterized by an austenitic γ matrix with homogenous and isotropic properties, as expected by the condition of quasi-hydrostatic pressing. The γ matrix includes a variety of fine-size precipitates that affect the grain-size distribution and the mechanical properties: a typical feature is represented by rounded or circular contours that are easily etched in a metallographic preparation of a sample, that are called prior particle boundaries (PPBs) [38-40]. As discussed in the following, these circular contours are formed by precipitates resulting from the phase transformation occurring during HIP at the surface of the powder particles. Grain boundaries mostly coincide with The PPBs mostly coincide with GBs although they cannot be distinguished from GBs by optical metallography. The rounded shape depends by the intrinsically small mechanical shear of particles during densification due to the hydrostatic pressing [7]. The shear of the bigger particles is furthermore reduced if they are surrounded by much finer particles. The optical metallographs of two as-HIP samples processed in the ST-HIP condition and in the T2-HIP condition are presented in fig. 3 a) and b), respectively: the presence of PPBs contours can be observed in both samples and constitutes an evidence of the thermal stability of such precipitates in the whole range of HIP temperatures considered in this investigation.

A deeper sight in the microstructure can be achieved by Scanning Electron Microscopy, in particular by the Backscattered-electron (BE) detecting mode that is sensitive to the mean atomic mass of elemental species of the material surface. This approach is particularly effective when the microstructure of the HIPped and heat treated samples is analyzed and the identification of precipitates is crucial. The BE-SEM image of a representative sample of the standard processing (ST-HIP-HT) made by powder p1 is shown in fig 4 a), while the fig. 4 b) presents the BE-SEM image of a representative sample processed by the increasing both HIP and solution treatment temperatures up to 1200°C (T2-HT2). A first aspect of primary importance is the observation of substantial very low, vanishing porosity, confirming the full density of the part. The precipitates found on the polished surface of these two samples are very similar: they consist in two broad categories distinguishable by the size and the mean atomic mass. Considering the fig. 4, such features are:

- coarser precipitates of the order of about 1 μm, characterized by a high average atomic mass (bright appearance in the SEM-BSE mode) as indicated in fig. 4 a);
- a network of chains of very fine precipitates (dimension of the order of 100 nm) appearing as dark spots in SEM analysis, as shown in fig. 4 b).

The latter type coincides with the Prior Particle Boundaries (PPBs) identified by optical microscopy. Such features tend to coincide with the grain boundaries, even if they are found crossing grains especially in sample HIPped and heat treated at the highest temperature. It is worth of noting that the PPBs can be constituted in part even by a residual vanishing porosity of nanometric size, as argued for example in diffusion bonding of Hastelloy C-22 in Ref. [19], as a result of impurities preventing the solid-state bonding.

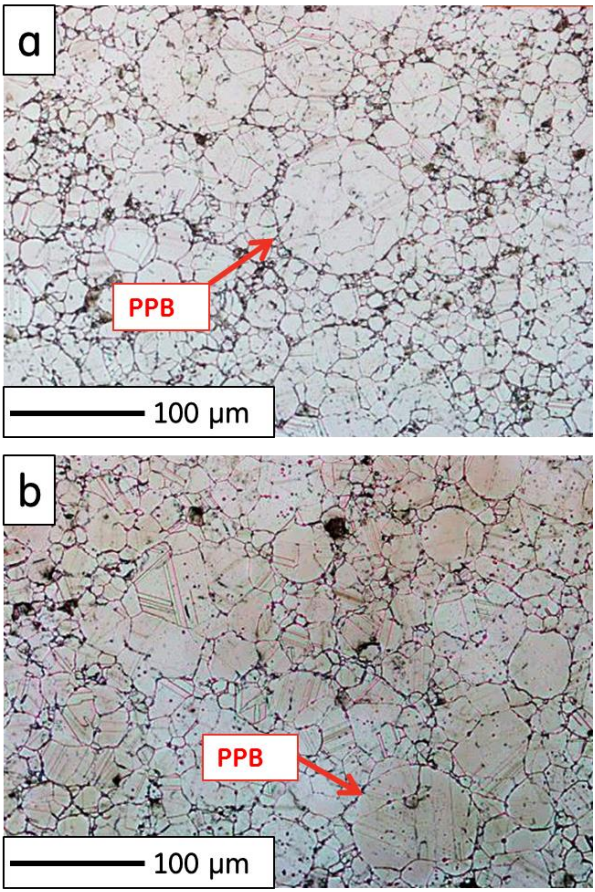

Fig 3: Optical metallographies of as-HIP p1 powder processed according to standard HIP parameters (a) and processed by increased HIP temperature T2 (b). (The picture was submitted for publication in Ref. [37])

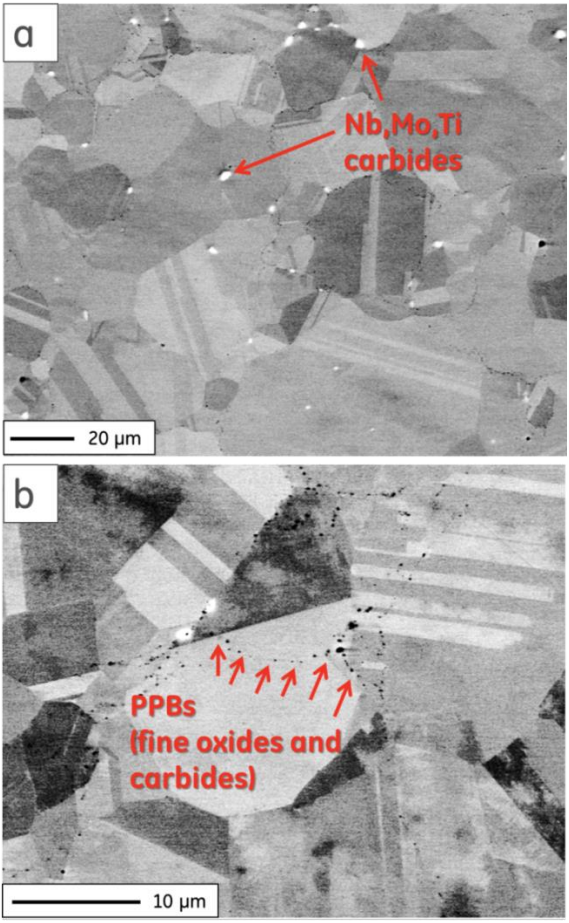

Fig 4: Backscattered electrons SEM images of HIP and heat treated samples processed according to ST-HIP (a) and T2-HT2 (b); in both cases the powder used is p1. The occurrence of carbides and PPBs is enlightened by red arrows. (The picture was submitted for publication in Ref. [37])

The coarser precipitates can be easily identified as primary carbides by their chemical analysis: a chemical mapping of a representative group of such precipitates achieved by a simultaneous SEM-EDS-EBSD analysis is presented in fig 5 for a sample processed in the standard condition and heat treated. Each precipitates

location in the maps is associated to the depletion of Ni and to the strong enrichment of Nb, Mo and Ti. Furthermore, the analysis of the EDS spectrum and the EBSD pattern in such precipitates indicate respectively an enrichment of C and a fcc crystal structure compatible with MC carbide. The depletion of Ni and the fcc structure exclude the identification as (Ni_3Nb) δ phase with an orthorhombic $D0_a$ structure, that can be present in Nb strengthened Ni-alloys both as thin platelets or globular shape precipitating preferentially at the grain boundaries. The SEM analysis then does not enlighten the presence of any recipitation of δ phase that is associated to detrimental effect of the mechanical properties of superalloys.

The Electron Backscatter Diffraction is a powerful tool in the analysis of the grain structure: it enables an accurate quantitative analysis of a large sample of very fine grained microstructure without any artifact due to a conventional chemical etching for optical metallography. This advantage is effective in presence of PPBs that cannot be unambiguously distinguished by GBs by optical metallography. The actual grain structure of the reference standard material (standard ST-HIP condition, standard powder high quality powder p1) is enlightened by EBSD analysis in fig 6 a): the black solid lines indicate the grain boundaries determined by a misorientation ≥ 10 ° between adjacent pixels. The EBSD analysis indicates a strong twins formation: in fig. 6 b) the same map as in fig 6 a) is shown without the coloring of the crystallographic orientation of the grains and the twin boundaries are represented by red lines. This microstructure is characterized by a bimodal grain-size distribution: rounded islands of coarser grains similar to what discussed before in the as-hip samples, included in a sort of matrix of much smaller grains more homogenous in size. This feature can be considered an important detail since the different GB density at the island boundary with respect to the fine grain matrix can be source of a weak point. This nature derives also from a second consideration: the perfectly rounded shape indicates an effective pinning of GB that can be associated to a prevented sintering/diffusion-bonding along the PPBs.

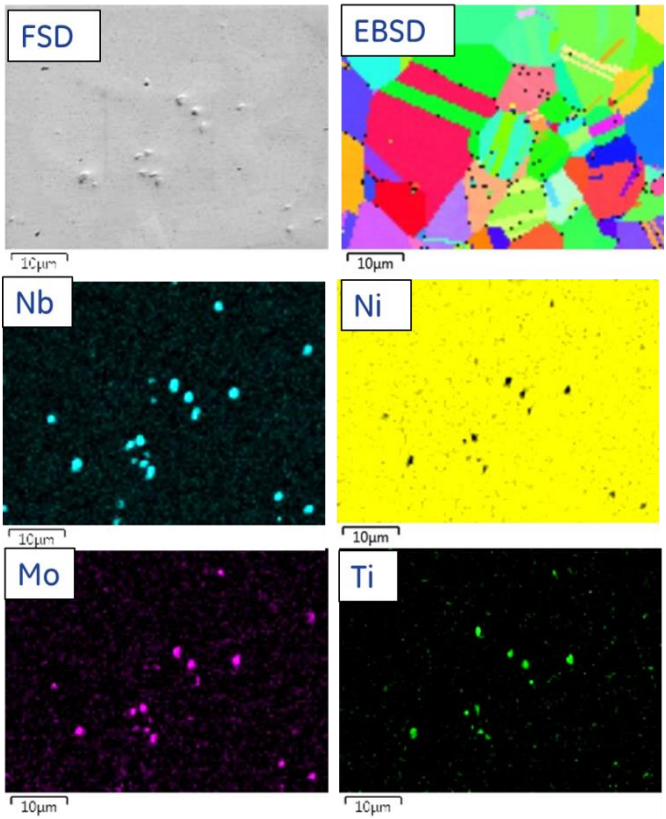

Fig 5: SEM-EDS analysis of a cluster of precipitates in a samples processed according ST-HIP and made by powder p1: the picture shows the SEM image (FSD), the EBSD crystallographic map of grains, the EDS chemical maps of Nb, Ni, Mo, Ti concentration in the SEM imaged area. (The picture was submitted in Ref. [37].

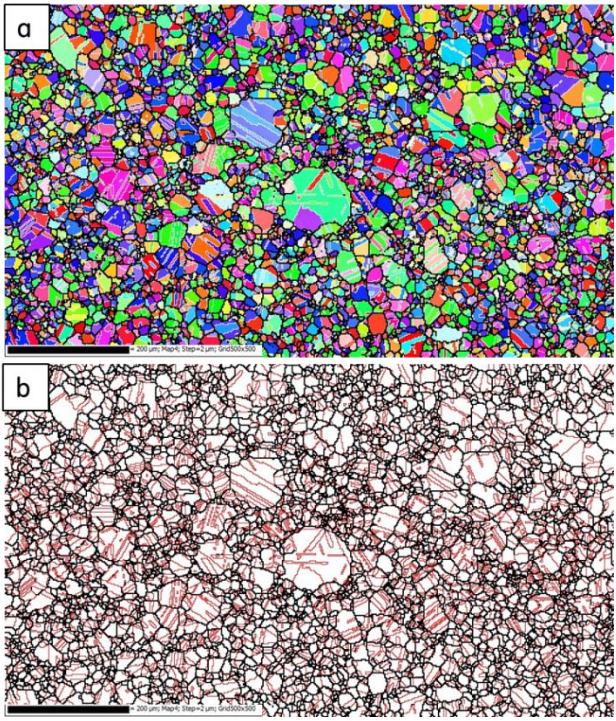

Fig 6: EBSD Inverse Pole Figure map of a sample processed according to ST-HIP condition by powder p1 (a); the figure (b) shows the reconstructed grain boundaries structure of the same area in (a) coloring in black the grain boundaries and enlightening in red the twin boundaries.

4.2 - Mechanical properties

It is usually established that powder metallurgy parts made by HIP are characterized by a high uniformity and isotropy of mechanical properties. This is an extremely important aspect when HIP technology is selected for net-shape manufacturing. This concept actually is partially true since it was found in this investigation that a localized significant degradation of mechanical properties can occur even in a part that exhibits globally outstanding properties. This fact is due to the thermodynamic transformations that act during the compaction time, involving the interaction between the capsule and the metal powder.

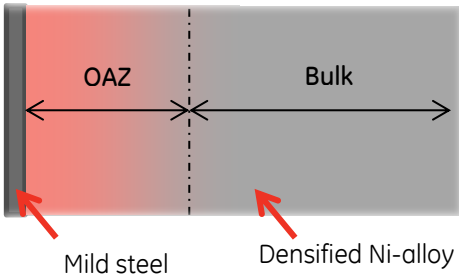

Fig 7: Sketch of an Oxygen Affected Zone in an ideal as-HIP consolidated capsule having still attached the external mild steel shell.

The most important effect is the systematic localized accumulation of oxygen in some point of full-scale consolidated parts. They are volumes of densified material extending inward several tens of mm from the external surface. An interesting aspect of this accumulation is that it is not associated to any accumulation of either nitrogen or carbon. Such volume portions are referred hereafter as Oxygen Affected Zones (OAZs) (see sketch in fig 7). The interpretation of this accumulation in described in section 4.3 . The individuation of OAZs and the analysis of their effect of mechanical

properties are fundamental for the implications in terms of design and reliability of a HIPped part. The investigation of the accumulation of oxygen in some point is also representative of the effect that the use of an oxidized powder can have regarding the mechanical properties.

4.2.1 - Room temperature tensile properties

The effect of oxygen accumulation on tensile properties can be enlightened by comparing the results of many tensile tests conducted by specimens sampled in OAZs and in the core of several HIPped part, manufactured according the same nominal processing condition, including HIP stage and post-consolidation quality heat treatment, and a metal powder with approximatively same properties. The data reported in fig 8 show the variability of the mechanical properties in the OAZs and in the reference material (cycle ST-HIP, p1-p2): such data are particularly important in the assessment of the reliability and the stability of a new manufacturing process introduced in industrial practices. The average values of the 0.2% Yield Strength and of the % Elongation in OAZs and in the core are then shown in fig. 8. The values are normalized, and are reported together with the lower specification limits (LSLs) for the most critical application of the alloy set for the company. These data show as the accumulation of oxygen doesn't affect the yield strength of the material but has a significant effect of the elongation leading to an appreciable reduction of elongation and to an increase in the scattering of results, so to an appreciable reduction of ductility. In both cases the results are promising for even the "weakest" location of a full scale industrial part is fully compliant with the prescribed design requirements. Another point to note is that yielding properties denote a very small scattering of results.

The analysis of the stress-strain curves of specimens sampled in OAZ and in the core indicates that the constitutive behavior is very reproducible, on the other hand the ductility is significantly impacted. The stress strain curve of 4 representative tensile tests of specimens cut in OAZs and in the core material are presented in fig. 8 with a constant offset along the stress axis. , They show that a standard material is characterized in all four cases by the same monotonic hardening that leads to the rupture without the drop in stress typical of the onset of tensile instability; less ductile

material just fails at lower values of elongation without any deviation from the constitutive behavior. The elongation of the sample is uniform and can reach relatively high values without exhibiting any necking.

Fig. 9 b) shows the stress-strain curve of two samples of p1 and p4 powder in the two available sizes, HIPped and heat treated according to standard conditions. As anticipated the properties of p4 powder are investigated as a representative material with a relatively high oxygen concentration and generally degraded mechanical properties. p4 material is softer than p1 standard material, the yield strength is 12.5 % lower than the p1, the ductility is also poorer and the strain hardening is lower. A significant improvement in ductility is found in the smaller size powder for p4 material.

The fig 10 shows the typical fracture surface of a tensile specimen fabricated according the ST-HIP processing and tested at room temperature. The general macroscopic behavior of the fracture can be defined essentially inter-particle and described by the individuation of two primary fracture mode that are always coexisting: a pronounced ductile fracture associated to extensive formation and coarsening of micro-dimples and a quasi-brittle debonding of isolated powder particles. In this last case the fracture surface is characterized by a much smoother profile. The fig 10 b shows the difference in the fracture surface at the boundary between a debonded particle and the irregular deformed matrix. Fig 11 presents the fracture surface of a tensile specimen produced by the powder p4 (fig 11b) compared with the standard reference sample (fig 11a): in this case the debonding mode is dominant. The fracture surface tends to be faceted as resulting of a mere mechanical compaction of ductile spheres (See german).

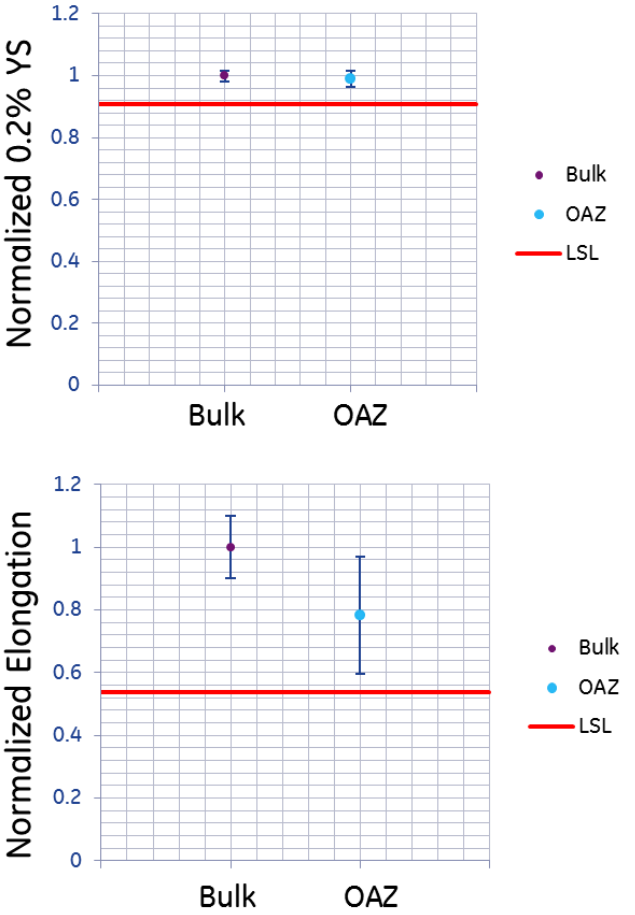

Fig 8: Tensile properties of the material processed according to ST-HIP by p1 and p2: a) mean 0.2 % yield strength and b) % Elongation in the core of the samples and in the OAZs.

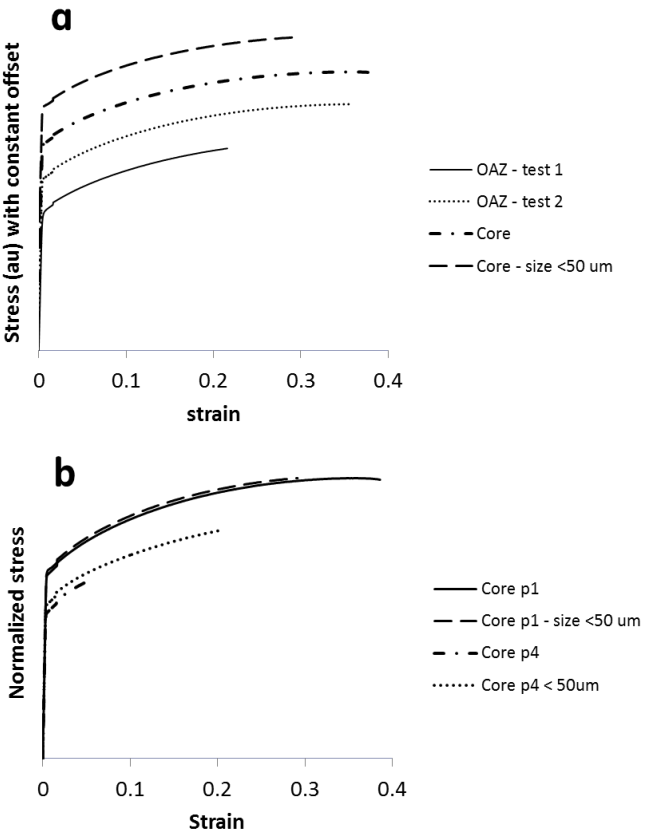

Fig 9: a) stress-strain curves of four tensile specimens sampled in the bulk of and in the OAZs of the material processed according to ST-HIP parameter by powder p1; the curves are presented with a constant offset in the stress axis to show the reproducibility of the constitutive behavior; b) comparison of the stress-strain curves for the consolidated p1 and p4 powder according ST-HIP conditions and using two different mesh sizes.

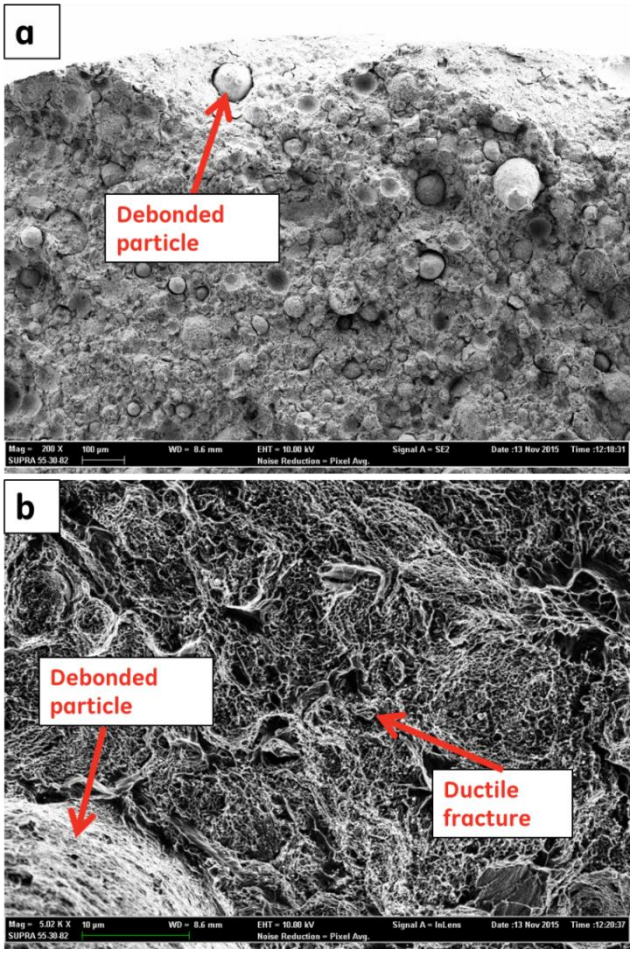

Fig 10: a) fracture surface of a broken tensile specimen obtained according to ST-HIP parameters and by powder p2; b) a magnification of the fracture surface at the boundary between a debonded particle and the embedding ductile matrix.

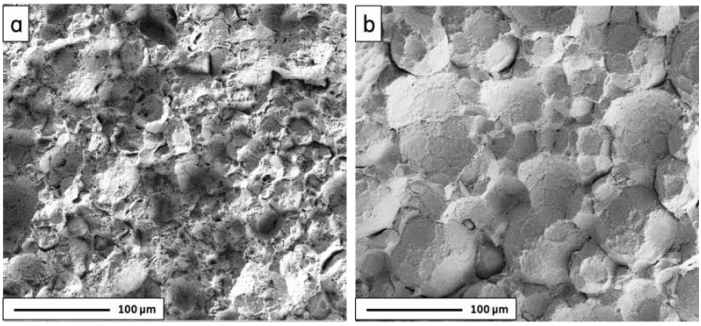

Fig 11: comparison of the fracture surface of two broken tensile specimens obtained according to the parameters ST-HIP by the powder p1 (a) and p4 (b).

4.2.2 - Room temperature Impact toughness

The accumulation of oxygen has a strong detrimental effect on the toughness on a standard reference material and makes it much more sensitive to the stress intensification of a notch. A very indicative analysis of such behavior is provided by the Charpy V-Notch testing. The results of a statistical evaluation of the absorbed energy measured in several parts (ST-HIP, p1 material) are shown in fig 12: the parts were sampled both in OAZs and in the cores. The data are normalized. This analysis shows that while the tensile behavior is not heavily impacted, the toughness response can be dramatically reduced.

If the measured impact energy of a large number of specimens is plotted over the measured oxygen concentration a behavior interpretable as a ductile-to-brittle transition (DTB) is found, in analogy to other classical DBT as in bcc steels. Many specimens were cut in the OAZs of several parts and the concentration of oxygen was measured in the same portion of material: this sampling has an intrinsic difficulty due to the distribution of oxygen in OAZs, which is present as inward diffusion gradients from surfaces. The values of the mean impact energy are plotted as a function of oxygen concentration in fig. 12 b. Since the Charpy measures were conducted in distinct laboratories according to the ASTM Standard E23 the error bars of the means represent the uncertainty expressed as:

$$\varepsilon = \sqrt{\sigma_{st}^2 + \sigma_{rt}^2 + \sigma_{rp}^2} \qquad \text{(IV.1)}$$

where σ_{st}^2 represents the standard deviation of the measurements and σ_{rt}^2 and σ_{rt}^2 are the uncertainties due to the repeatability and the reproducibility of the test as reported in the ASTM E23 standard.

The macroscopic aspect of a typical fracture surface of broken Charpy specimens of the standard reference material is very similar in many aspects to the tensile fracture surface. The main aspect is that also in Charpy specimens the fracture occurs preferentially along the PPBs, so the fracture is preferentially interparticle. In fig. 13 a) a magnification of the fracture surface of a Charpy specimen is shown in order to have a sight of the microstructure. The surface appears partitioned in areas of marked ductility, identified by coarser dimples, and smoother areas with a quasi-brittle look. A high magnification imaging of the surface shows that smooth areas exhibit also submicrometric -dimples associated to the formation of nano-voids embedding inclusions. These inclusions, as will be discussed widely in the following, are the constituents of the PPBs, already identified in the analysis of the microstructure. Similar inclusions are found systematically in most of the fracture surface and can be identified as a general feature of the fracture surface of this P/M material.

A second fact is that the mechanical response of the material is the result of a heterogeneous behavior at the PPBs with a portion of volume exhibiting a ductile response while the remaining portion acts as quasi-brittle.

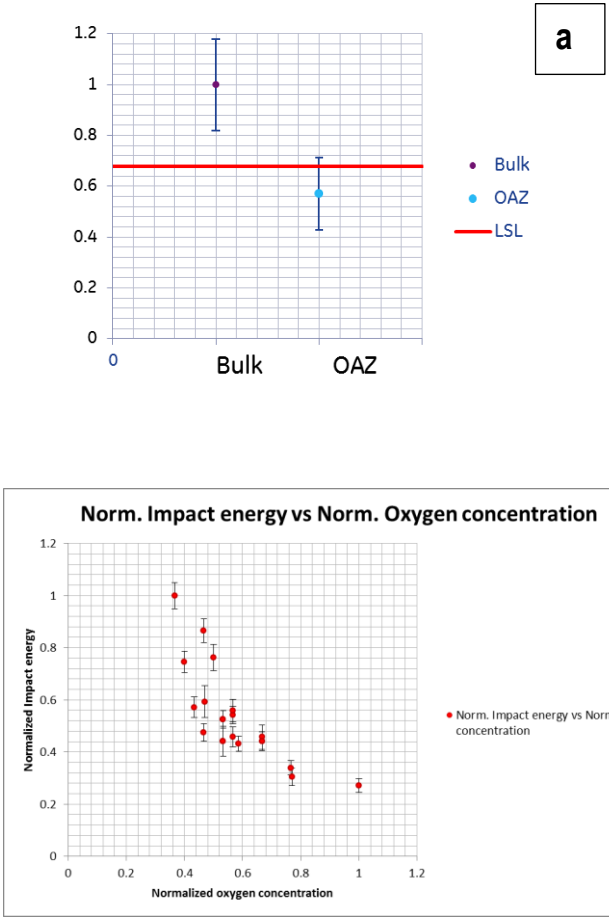

Fig 12: a) mean absorbed impact energy in Charpy V-Notch tests conducted on samples processed according ST-HIP parameters with powder p1; the specimens were sampled in the bulk and in the OAZs of several parts; b) measured absorbed impact energy of several Charpy V-Notch samples over the measured oxygen concentration, the process condition was ST-HIP with powder p1.

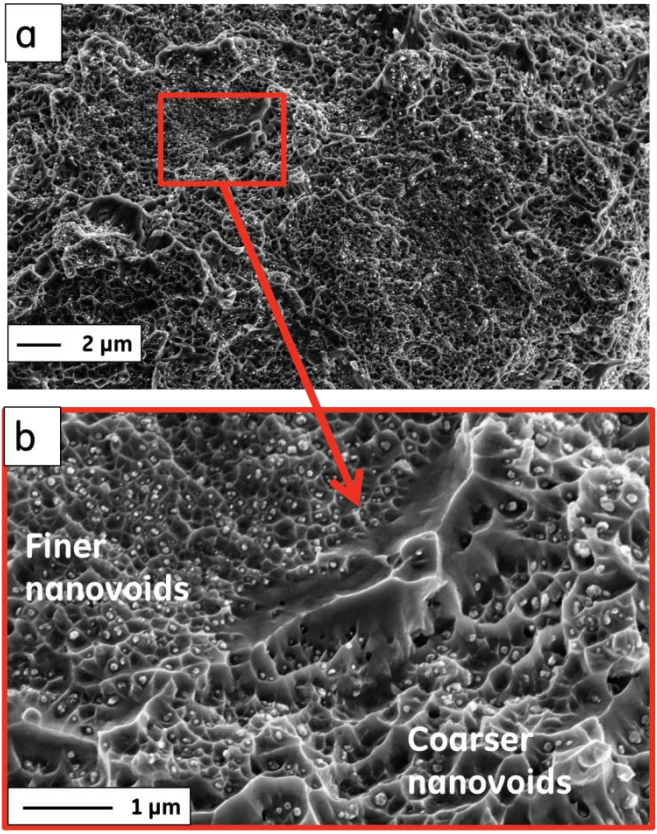

Fig. 13: a) fracture surface of a broken Charpy V-Notch specimen sampled obtained by ST-HIP processing with powder p1; b) high magnification of a particular of the fracture surface showing the formation of submicrometric voids with embedded PPBs precipitates.

The use of instrumented Charpy-pendulum tells us many information on the toughness of the material. In fig 14 the load defection curve of the standard reference material (ST-HIP, p1 powder) compared with the weak case-study material produced by p4 (ST-HIP) is shown. The data demonstrate that in both cases the propagation is not truly brittle even if the slope of the propagation step of the curve is a bit steeper for the p4 material. In the p4 material the peak load, indicating conventionally the crack nucleation stage, occurs at appreciably lower load than the

reference material. The fig. 13 reports other two load-deflection curves of the two materials obtained by the consolidation a finer sieving of powder with the same processing parameters (indicated with the term small in the plot): no appreciable deviation from the coarser particle size is observed. This result suggests that the presence of bigger poorly bonded particles doesn't affect significantly the global response of the material.

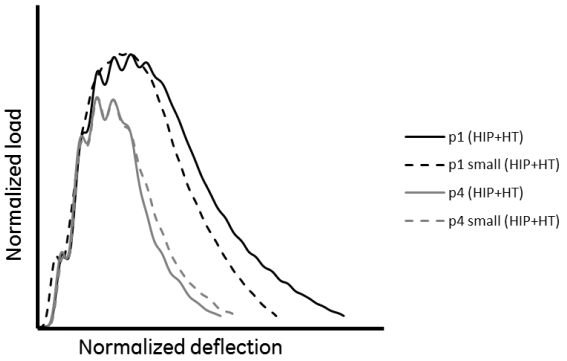

Fig. 14: Load-deflection curves of instrumented Charpy V-Notch tests with specimens obtained according to ST-HIP parameters with two particle size distributions of powders p1 and p4.

The reduction of ductility and toughness are related to the fracture mode of this material. The analysis of the fracture surface of tensile and CVN specimens reveals that the fracture occurs preferentially along the PPBs as suggested by the rounded shape of the cavities and the protrusions representing the fracture path.

The results discussed so far demonstrate how the formation of PPBs affects the mechanism of the fracture. For this reason in the following section the structure of PPBs is analyzed in a more general discussion of the the chemistry and of the structure of the metal particle surface as well as the solid-state surface phenomena occurring during HIP that affect the final structure of the interface among particles.

4.3 - Phase transformations at particle surface during a HIP consolidation

The chemistry and the microstructure of the surface of the consolidating metal particles is the result of their production process and of the solid states transformations occurring during a HIP cycle. The sintering of metal powder is strongly affected by the oxides present on the metal powder at the onset of densification. Such oxides are responsible of retardation as well as of a prevented sintering. As discussed in chapter 1, most of the densification in HIP is due to the deformation (both plastic yield [4] and power law creep) and this stage of densification if pretty rapid. So most of the HIP cycle is elapsed with the compacting powder in a stage of diffusion bonding at the surface of the particles. The analogy with solid state diffusion bonding is then very useful to understand the thermodynamic transformation acting at particle surfaces.

The constitution of OAZs described in previous section enlightened that oxides can be due to intrinsic factors of the raw material as well as to “extrinsic” factors (depending on the sintering condition), operating during the HIP cycle. The two source of oxidation are discussed in the following.

4.3.1 - Formation of PPBs:

4.3.1.1-Thermodynamics of surface oxide of metal particle in a closed system

It is well established that the existence if oxide layer on the metal surface to bond by solid-state diffusion bonding prevents or partially deteriorate the bonding effectiveness. The way to improve the bonding is based on methods to mechanically break or thermodynamically destabilize the oxide layer for a complete dissolution. The resistance to dissolution of the oxide layer depends strongly on its physical/chemical stability in the condition of the process: the temperature, the local chemical composition and the local atmosphere. According to Ref. [44] there are three main general behaviors found in metallic materials at the bonding interface in a diffusion bonding process:

1) (titanium type) stable oxides in metals having a high oxygen solubility tend to dissolve and diffuse in the matrix;

2) (iron type) oxides tend to condense and form inclusions that progressively are dissolved in the matrix;

3) (the aluminum type) the oxides are very stable and cannot be either dissolved or decomposed.

Even thermodynamically stable oxides at a certain process temperature and chemical composition can be destabilized by a proper selection of the process atmosphere. This is a standard practice in conventional sintering of many materials using dedicate reducing atmosphere with defined partial pressure ratio of CO/CO_2, H_2/H_2O or either vacuum [45,46].

The destabilization of oxides by the control of a reducing atmosphere cannot apply to a HIP process since in this case the consolidation of the powder occurs in a sealed capsule without the possibility to control the atmosphere. The atmosphere can be determined just at the beginning of the process by operation of degassing preceding the sealing. Therefore, at the beginning of a HIP cycle the atmosphere inside the capsule is a nominal low vacuum. Since the capsule represents a closed system, when the part is heated two main phenomena start: 1) residual moisture or oxygen chemically bonded to the particle surface is desorbed; 2) the residual oxygen in the vacuum atmosphere start to oxidize the particle surface until an equilibrium partial pressure of oxygen is reached. This pressure is determined by the equilibrium condition of the red-ox reactions of the between the base metal and the relative oxide, according to the law [47]:

$$\Delta G^0 = -RT\ lnP_{O_2} \qquad \text{(IV.2)}$$

ΔG^0 represents the change in the Gibbs free energy associated to the formation of the metal oxide, R is the ideal gas constant and, T the temperature and P_{O_2} the equilibrium oxygen partial pressure.

Therefore, the equilibrium oxygen partial pressure is expected to be determined by the most stable oxide species formed. In a Ni-base alloy as the N07626, the oxidation behavior is not simple due to the chemical composition that is

prone to selective oxidation, so several oxides are actually forming during an oxidation stage [48]. The powders produced by inert gas atomization are usually covered by a thin layer of oxide with a thickness of the order of 10 nm. The oxidation occurs at the atomization stage itself due to the residual oxygen present in atomizing gas and in the fast cooling inside the collection chamber. Ref. [49] characterized the oxide layer on inert gas atomized aluminum powder finding that the thickness is not uniform and island can form in a single particle, but the oxide thickness is generally similar for all the size distribution of the particles. Ref. [50] reported the characterization by Auger spectroscopy of a Ni-base powder produced by inert gas atomization, demonstrating a surface enrichment of element associated to stable oxides (Ti, Al, Cr). In the case of the alloy N07626 the structure of the initial oxide can be reconstructed by the Ref. [51] and by the consideration that the oxidation during the atomization is a too fast process for the creation of a protective barrier of stable oxides forms. So an important portion of NiO and of the Spinel $NiCr_2O_4$ oxides is expected constitute the initial layer of oxide together with Cr_2O_3. Since the Ni alloy contains elements forming most stable oxides, the decomposition of $NiO/NiCr_2O_4$ layer will be put in place for the precipitation of Cr_2O_3, Al_2O_3 oxides. The analysis of the oxidation behavior of IN625 by Ref. [50] indicated that even other oxide can form, like NbO_2.

As demonstrated by Ref. [50] an initial less stable $NiO/NiCr_2O_4$ oxide layer can be replaced at higher temperature by Cr_2O_3, TiO_2 and NbO_2 in low oxygen partial-pressure oxidation conditions.

As discussed at the beginning of this chapter, in metal like iron or copper the oxide layer tends to condense and dissolve in the parental metal. This is argued to be the case of a Ni-Cr base alloy like N0726 exhibiting a significant fraction of NiO oxide at the beginning of the HIP transformation. According to Ref. [52] the nickel has a solubility of 0.05 atomic % at 1273 K that corresponds approximately to 0.014 weight %. The lowest oxygen concentration attainable in commercial high-quality Ni-base powder is in the range of 0.01-0.03 wt %. These considerations suggest that just a portion of the oxygen present in the particle surface can dissolve in the bulk metal up to the complete saturation of the matrix by oxygen. If the oxygen solubility limit is overcome by higher concentration of oxygen, no dissolution of oxides occurs

whatever the selected HIP conditions: the oxidized material of OAZs and the powder p4 are expected to be concerned by this phenomenon. On the basis of a similar concept Munir et at proposed a maximum thickness layer that can be dissolved during sintering by pure diffusion.

4.3.1.2 - Precipitation of carbide at PPBs

A second phase transformation contributes to the formation of PPBs: the precipitation of carbides. There is a wide literature about the structure of PPBs in nickel alloys that enlighten the preferential precipitation of high-solvus carbides like NbC or TiC [53-55]. Several authors suggest that oxides themselves act as nucleation site for the precipitation of the carbides. The formation of high-solvus MC carbide is particularly effective in material rich of strong carbide former like Nb in Inconel 718. Due to the similarities in the chemical composition between Inconel 718 and the N07626, the structure of PPBs is interpreted on the base of the data existing for the former. A recent investigation of PPBs in powder metallurgy Inconel 718 was provided by Ref. [38] that identified MC carbide as the main constituent of PPB. In previous analyses Ref. [55] identified both MC carbides and Al_2O_3 precipitates at the PPBs.

4.3.1.3- Experimental analysis of PPBs precipitates of HIP N07626

The analyses of the literature find agreement with the experimental investigation conducted in this research about PPBs precipitates by EDS microanalysis. A representative EDS spectrum of a PPB precipitate in the standard material is compared with the spectrum of the matrix in fig. 18. The comparison of the two spectra enlightens a marked intensification of the characteristic emission peak of O, C, Nb and Al, in perfect agreement with the interpretation of inclusions of carbides and oxides. Although the Al peak is observed, it not certain that all the available oxygen precipitated as alumina.

The effectiveness of the solid state transformation at the particle surface can be illustrated by the fig. 16 showing the comparison of the load-deflection Charpy curves of the standard reference material and of the oxidized p4 powder in the as-HIP status and after the quality heat treatment. In the case of p4 material (that is

characterized by 50% more oxygen concentration than p1) the curve of the as-HIP sample indicates the occurrence of a brittle fracture (note the vertical drop of the curve), while in the ST-HIP state the crack nucleation occurs at higher load and the crack propagation step is appreciable. In the case of the reference material (ST-HIP-p1) there is no a so marked difference in the behavior of the load-deflection curve. This result can be interpreted as the demonstration of the retardation of the diffusion bonding in the p4 case. The bonding strengthens during the following solution heat treatment.

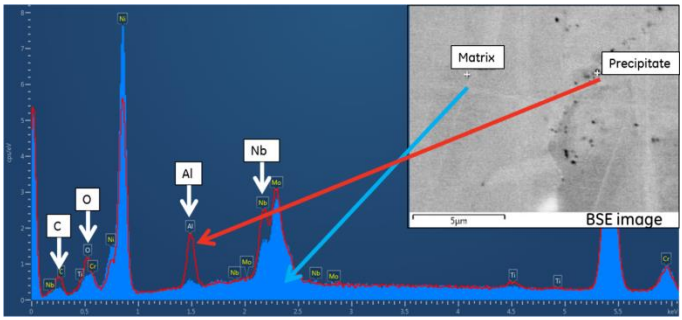

Fig. 15: EDS spectrum of a PPB precipitate (red spectrum) compared with the austenitic matrix (blue spectrum) of a sample processed according to ST-HIP parameters with p1 powder; the spots of the EDS analysis are illustrated in the caption on the top-right corner. (Picture submitted for publication in Ref.[37])

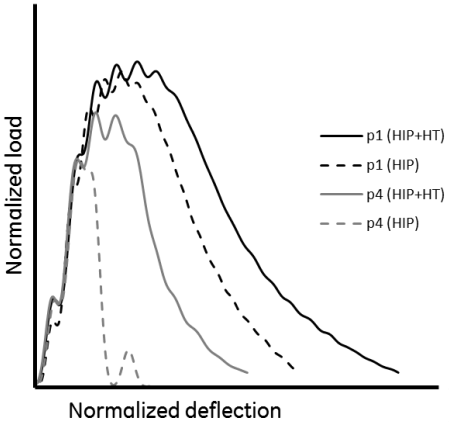

Fig. 16: Load Deflection curves of the instrumented Charpy V-Notch test of as-HIPed and HIPped plus heat treated samples processed according to standard HIP parameters with powder p1 and p4.

The chemical products of the phase transformations taking place during HIP can be appreciated in fig. 17 by the comparison of SEM imaging of a representative p4 powder particle before HIP (fig. 17a) with the fracture surface of broken Charpy specimen from the as-HIP p4 sample (c). The caption in fig. 17 b is a high magnification of the particle surface showing a smooth surface characterized by a dendritic structure; no nanometric precipitate is found of the surface, the oxide layer cannot be imaged. The fracture surface of the Charpy specimen shows a strong formation of precipitates.

The comparison of the surface of the powder used to fabricate the reference material with the fracture surface of broken charpy sample after the full heat treatment is presented in fig. 18.

The identification of PPBs precipitates as MC carbides and stable secondary oxides is particularly important in term of their thermal stability, and then in the selection of a proper quality heat treatment. Ref. [43] demonstrated that the dissolution of NbC in polycrystalline nickel alloys occurs at a temperature above

1270°C. This motivated also the proposal of a super solvus solution treatment of Inconel 718 in Ref. [56] to dissolve the PPBs. These data are consistent with the experimental evidences of Ref. [38] that shows traces of PPBs even after a heat treatment at 1260°C and with our experimental investigation. In the present investigation in samples produced by any powder and HIPped and solution treated at 1200°C, the PPBs are still found. The main difference with standard material is that the PPBs are increasingly separated by GBs.

The formation of thermally resistant precipitate at the PPB, mostly coinciding with GBs, is not necessarily a defect to be removed. If present in the proper quantity such features can contribute to keep a fine grain structure by pinning the GBs. On the other hand, a super solvus solution treatment can produce a massive grain growth losing the benefit of a fine homogeneous structure.

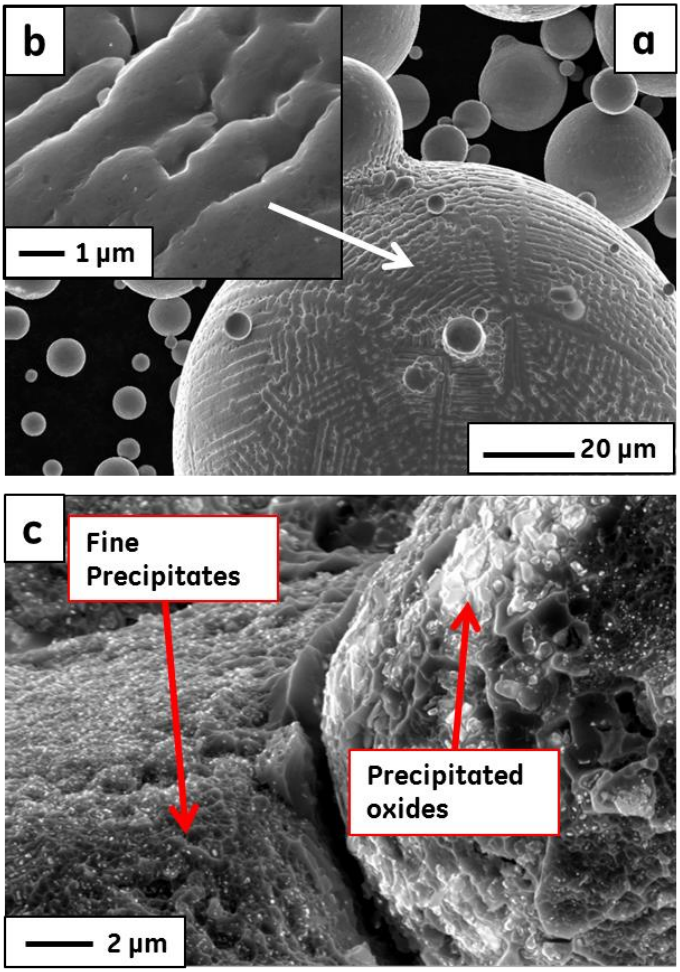

Fig. 17: a) SEM image of loose p4 powder; b) high resolution magnification of the particle surface; c) precipitates in the fracture surface of a broken Charpy specimen obtained from an as-HIPped sample (standard HIP conditions) made by powder p4.

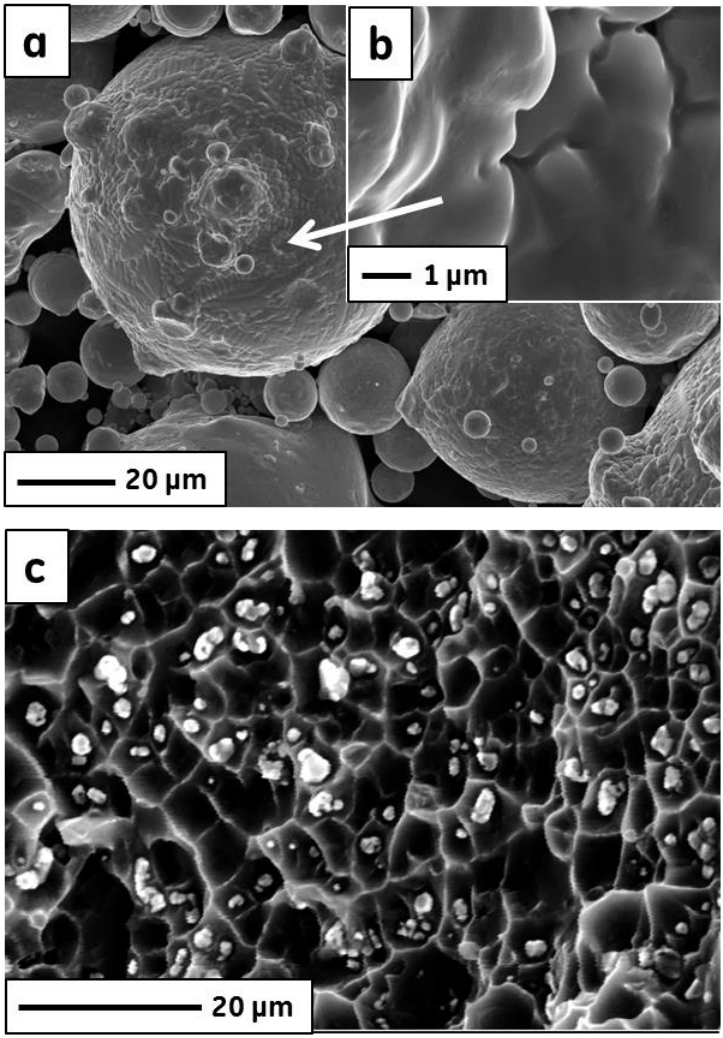

Fig. 18: a) SEM image of loose p1powder; b) high resolution magnification of the particle surface; c) precipitates in the fracture surface of a broken Charpy specimen obtained from an HIPped and heat treated sample (ST-HIP conditions) made by powder p1.

4.3.2 - Reduction/Oxidation phenomena during HIP.

As discussed in previous section during the heating up of the HIP cycle and before the closure of the porosity (i.e. until the porosity results still connected) the oxygen partial pressure will depend by the most stable oxide formed or forming. This concept is particularly important since if less stable foreign oxides are present inside the capsule, even not due to the particle powder, they can reduce and release O_2 that can further oxidize the more stable oxides. This is one of the two mechanisms proposed to explain the formation of OAZs.

Suppose that, due to the favorable conditions for selective oxidation of Cr_2O_3, the oxygen partial pressure is determined by the equilibrium O_2 partial pressure for Cr_2O_3 at the process temperature inside the closed capsule. The capsules used for the cycles were fabricated by mild carbon steel. This metal usually forms a thin nanometric passivating layer of iron oxide at room temperature. But if the metal is heated, like in the welding operation of the assembly, much thicker oxide layer can form, even if the welding operations are performed in protective atmosphere. The idea proposed is based on the difference in thermodynamic stability between iron oxide in the capsule and Cr_2O_3 or more stable oxides present on the surface of the Ni-alloy powder: the lower equilibrium partial pressure of Cr_2O_3 reduces Fe_2O_3. A glance to the difference of oxygen partial pressure between the Fe_2O_3 and the Cr_2O_3 can be appreciated by the plot in fig. 19 that is adapted from Ref. [45], The plot identifies the relation of the partial pressure of several oxide species in a stainless steel with the temperature of the redox reactions, showing all along the whole range of considered temperature the oxygen partial pressure of Cr_2O_3 is much smaller than for the iron oxide.

The increment in temperature during the ramp up of the HIP cycle affects the system by enhancing the destabilization of the iron oxide and increasing the oxidation rate of the Cr_2O_3 oxide according to the Arrhenius-type dependence of its diffusion coefficient [47]. The more the Cr_2O_3 oxides grow, the more the equilibrium of the system influences the oxygen destabilization. The resulting desorbed oxygen diffuses in through the channels of connected porosity. The dimension of tens of mm of thickness of OAZs confirms that this extrinsic oxidation is due to the action of gaseous diffusion rather than solid-state diffusion. The latter phenomenon would

have led to diffusion path of the order of tens of μm, as for example investigated for surface diffusion of oxygen in nickel in Ref. [57]. The gaseous diffusion process is time-constrained by two factors:

1) as soon as the temperature of the cycle rise up the densification is enhanced and the porosity tend to be disconnected;

2) the diffusion of the gases should be described as Knudsen diffusion in a porous medium since the free-path of the gaseous species are determined by the particles in the space.

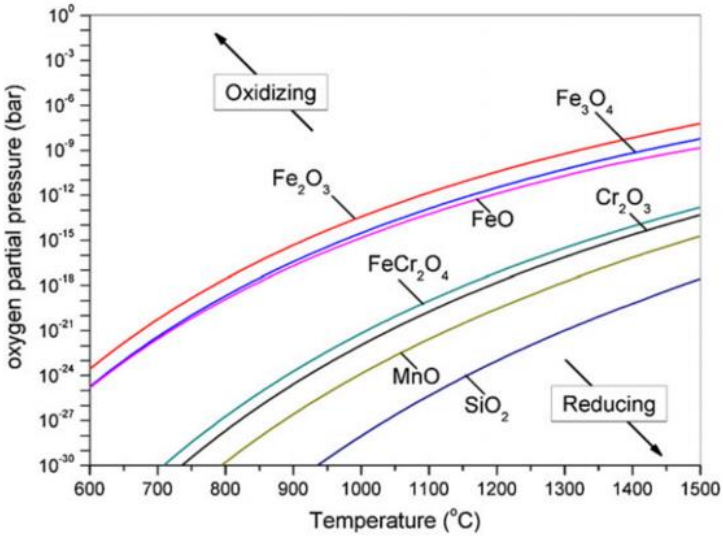

Fig. 19: equilibrium oxygen partial pressure of typical oxide species present in chromium-alloyed steel, adapted from Ref. [45].

An experimental confirmation of this interpretation is provided by the analysis of sampled interface capsule/consolidated Ni-alloy in HIPped parts. It was found that relatively thick oxides may be present at the interface capsule/powder. The example of the composition of such an interface in the consolidated condition of the capsule is provided in fig. 20 where the SEM image of the interface is shown with the EDS chemical mapping of principal elements involved in these red-ox reactions. The EDS analysis reveal the formation of 25 μm thick regions with prolonged Cr oxide (see

superposition of Cr and O signal) and no iron oxide. Since Cr is present only in the Ni-alloy, these oxides formed during the HIP cycle from the decomposition of previously formed iron oxide. The reconstructed picture is compatible with a partial decomposition of the steel oxide layer occurred via desorption in a first stage when porosity is still connected and by solid-stated transformation in the final stage when the porosity is closed.

In order to have a very approximate estimation of the impact of effect of the decomposition of iron oxide, consider a 2 dimensional infinite plate of iron oxide of thickness *t* and density ρ_{ox}, whose oxygen can diffuse in one direction in a layer of thickness l of porous Ni-alloy with fractional density *D* (actual density of the alloy is ρ_{Ni}). For simplicity let's suppose that such accumulation of O_2 is constant along *l* (actually a diffusion gradient should be adopted):

$$l = \frac{\rho_{ox}\mu_{ox}}{\rho_{Ni}} \frac{1}{c_{ox}D} t \qquad \text{(IV.3)}$$

where c_{ox} is the concentration of accumulated oxygen and μ_{ox} is the mass fraction of oxygen in the iron oxide. If the concentration c_{ox} sufficient to deteriorate the mechanical properties is very small the multiplication factor of *t* can be several orders of magnitude.

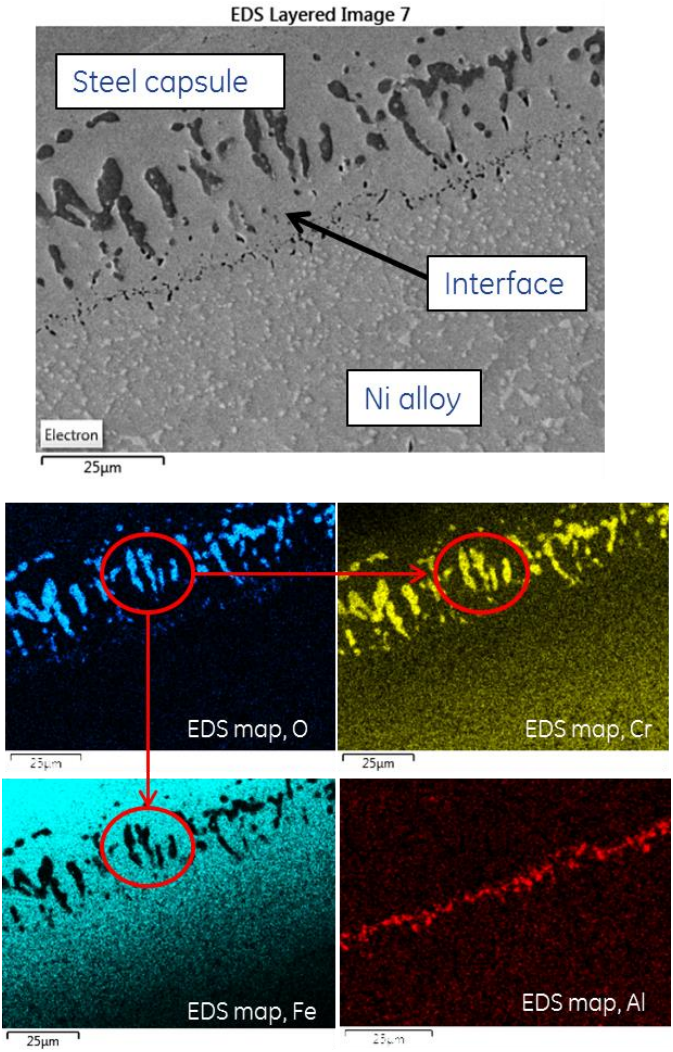

Fig. 20: EDS chemical mapping of the interface between the mild steel capsule and the consolidated Ni-base powder in a HIPped sample, processed according to ST-HIP parameters. The reference SEM Image is shown on top, in the bottom of the picture the maps of O, Cr, Fe and Al concentration of the same surface are shown.

4.3.3 - Oxidation by residual entrapped moisture

A second mechanism can operate inside the sealed capsule as responsible of the accumulation of oxygen in OAZs. This mechanism has not to be thought as alternative to the reduction of weak oxides. The basic concept is that the accumulated oxygen can be the result of an incomplete elimination of moisture or condensation present on the surface of the metal powder during the evacuation stage of the preparation of the capsule. It has been reported that H_2O vapor can be chemically bonded to the metal powder and desorb only if a warm outgassing is promoted. This is demonstrated for aluminum powder in Ref. [58].

If a residual content of water vapor remains trapped inside the capsule, it can desorb in the early stage of densification (at connected porosity) and contribute to an oxidation of hottest zones. The preferential oxidation of just the periphery of the volume can be explained by the consideration that inside a capsule of powder significant gradients of temperature can form due to the low thermal conductivity of the powder material relatively to the bulk reference, being just a fraction of it as for example discussed in Ref. [59]. This effect is further amplified by the consideration that the thermal conductivity of a Ni-base alloy is relatively low. Therefore, in the transient heating stage of the capsule inside the HIP furnace the periphery can be hundreds of degrees hotter than the interior of a capsule. Since the oxidation rate on a Ni-base material depends strongly on the temperature, the periphery of a capsule is oxidized before the core, consuming all the available oxygen in the capsule atmosphere.

A glance to the outgassing behavior of this PM Ni-alloys can be given by the analysis of the chamber pressure measured during a set of SPS experiments. The chamber pressure of the SPS cycle with varying maximum temperature already presented in chapter III are shown in fig. 21 together with a trend line of the temperature. The initial vacuum pressure decreases in the un-controlled heating stage of the cycle until a first peak is found at about 0.5 T max: since this temperature is too low to represent massive desorption of oxidation product or evaporation of metal constituents, it has to be associated to the moisture degassing.

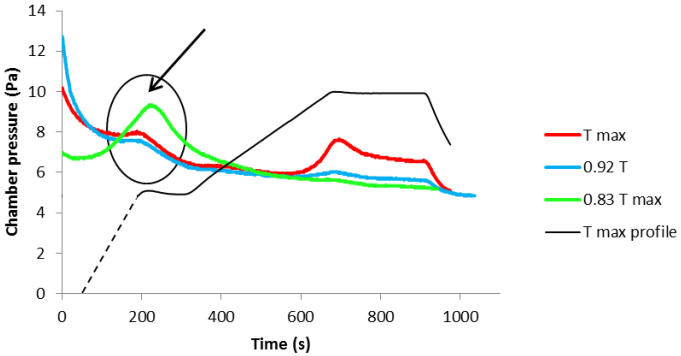

Fig. 21: SPS chamber pressure measured in the course of the SPS experiments sps1, sps2 and sps3.

4.4 - Fracture mechanics of PM materials

4.4.1 - Analysis of fracture surface

The reduction of ductility and toughness are related to the fracture mode of this P/M material. The analysis of the fracture surface of tensile and CVN specimens reveals that the fracture occurs preferentially along the PPBs as suggested by the rounded shape of the cavities and the protrusions representing the fracture path.

The appearance of the fracture surface is complex: the macroscopic aspect is characterized by the coexistence of areas with smooth surface and surrounding areas of irregular shape where plastic deformation is more pronounced. The smooth surfaces appear both as rounded convex and concave, partially faceted, resulting from the de-bonding of prior particle spherical shape and the limited shear deformation acting in HIP. A comparison of the tensile and the Charpy fracture surface is provided in fig. 21: a high magnification imaging of the fracture surface reveals a key aspects of the fracture mode, i.e. the spread of fine nanometric precipitate embedded in submicrometric-cavities with onset of nano-dimples formation. Both in areas of marked plastic deformation and in smooth debonded surfaces the formation of nano-voids at the PPBs inclusion and their coalescence through the formation of micro-dimples seem to represent a general micro-ductility behavior. The structure of the formed nano or micro-voids is complex, exposing areas with heterogeneous void size. Due to the density of nano-inclusions stacked by even less few hundreds of nm, the nucleated nano-voids easily interact coalescing into coarser micro-voids. The size of the micro-voids is approximately equivalent to the mean spacing of the inclusions. Clustering of nano-inclusions frequently occurs, leading to a local drastic reduction of the plastic response associated to finer nano-voids and very limited developing of nano-dimples.

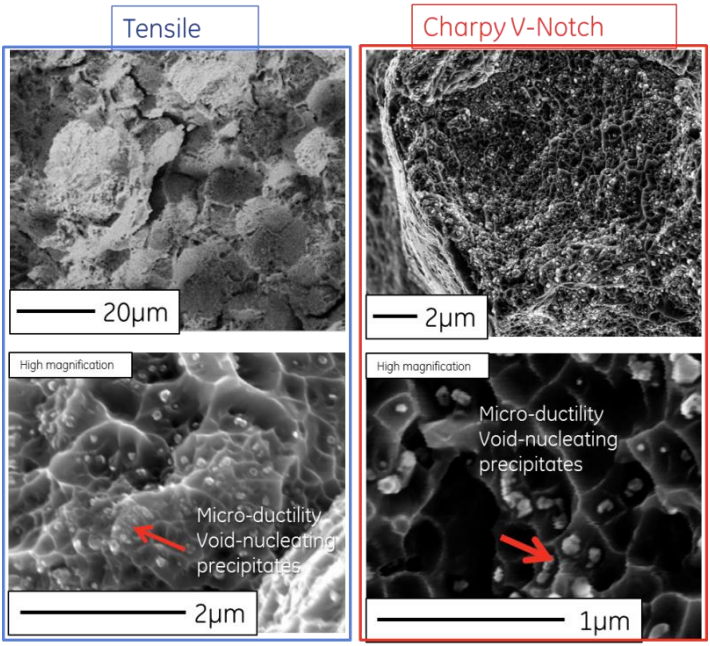

Fig. 21: representative fracture surfaces of a broken tensile specimen (left) and a broken Charpy V-Notch specimen (right) obtained by consolidation of powder p1 according to ST-HIP parameters. In both cases the fracture surface is characterized by formation of submicrometric voids embedding fine precipitates.

The fig. 21 compares the nano-void structure in broken charpy specimens of a low toughness reference material (above) to the toughest one (below). The tougher sample exhibits coarser voids, while the void coalescence is less marked in the second one. The ability in coalescence denotes more energy spent in the void-growth stage and then a bigger plastic energy spent in opening a crack, so a tougher behavior. If the above described structure of fracture surface is mostly uniform in the standard material an interesting behavior is found in material p4. In this case the ductile response is dominant just at the triple joints among particles, where coarser micro-voids are found, and a sudden change to apparently quasi-brittle fracture in the central zone of a compaction facet. In this areas just nanometric void are found.

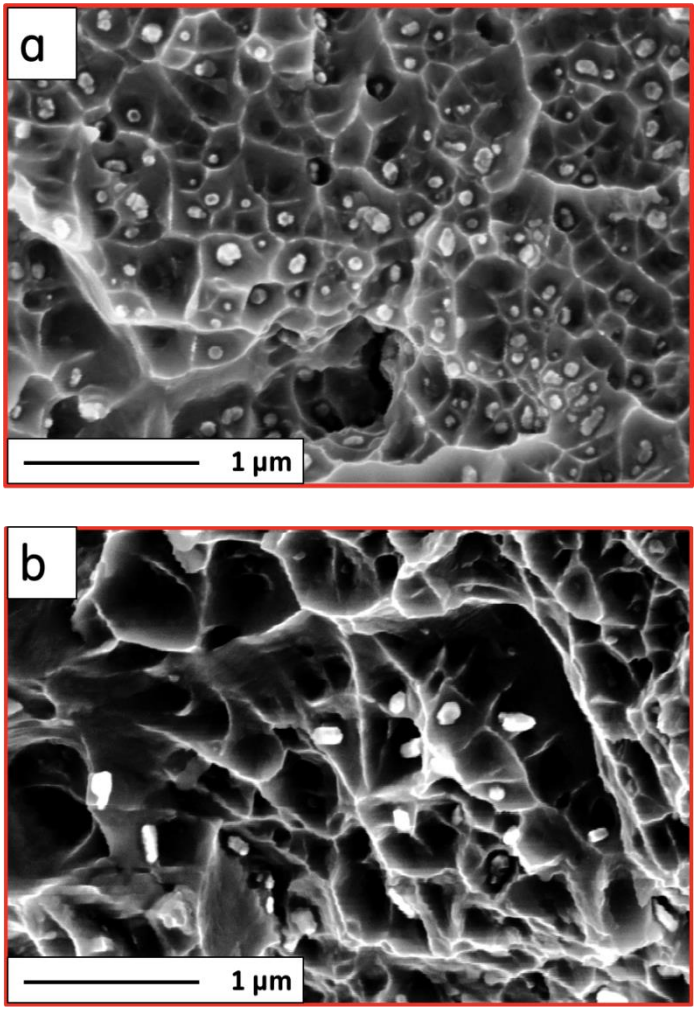

Fig. 22: fracture surfaces of two broken Charpy V-Notch specimens with different values of absorbed impact energy: a) low impact energy; b) high impact energy. The material was obtained by consolidation of powder p1 according to ST-HIP parameters.

The aim of this section is to provide a general fracture mechanical model of the powder metallurgy full-dense Ni-alloys on the basis of the experimental evidences so far described. The section describing the mechanical properties enlighten that the toughness of the material is strongly affected by the oxygen concentration. The oxygen is associated to the thin oxide of the metal particles that transform during the HIP with an agglomeration at the PPBs and constitute the precipitates found in the fracture surfaces. Such inclusions act as nucleation site for nano-voids with aspects that suggest a micro-ductile fracture mode. The fracture mode can be determined in principle by the inclusions as well as by other effects as a reduction of the cohesive energy at the GBs coinciding with PPBs.

4.4.2 - Ductile fracture mechanism by inclusion debonding: damage accumulation and crack propagation

This section aims to clarify the possible mechanisms that relate the density of inclusions at PPBs and their characteristic with the crack formation and the crack propagation in simple mechanical systems.

Since the fraction of oxygen dissolved in the matrix during HIP is not known, let us suppose that all measured oxygen is present in the HIP alloy as spherical oxide nano-inclusions of diameter *a*. Let us assume that the PPB can be represented by spheres of mean radius R, corresponding to the prior metal powder. Then the surface density of inclusion φ at a PPB surface is:

$$\varphi = \frac{\rho_{Ni}}{4\pi\mu_{ox}\rho_{ox}} \frac{R}{a^3} c_{ox} \qquad \text{(IV.4)}$$

with ρ_{Ni} and ρ_{ox} are the density of the Ni-alloy and the oxides, respectively; μ_{ox} is mass fraction of oxygen in the oxide and c_{ox} is the measured concentration of oxygen in the consolidated sample expressed as mass fraction. This relation indicates that density of inclusions is proportional to the oxygen concentration; smaller inclusions determine a higher density and that a coarse powder is exposed to higher density of inclusions than a finer one. This latter fact depends on the much smaller specific volumic surface (total surface/total volume) of a coarser powder.

In this investigation an ibrid model is proposed that is based on the analogy with the particulate reinforced metal matrix composite, since a PM material can behave as a MMC in the thin layer along the PPBs. In this case an important remark has to be pointed out; the HIPped materials behaves as MMC [60,61] just in a small portion of their volume. On the other hand HIPped materials for several aspects can be treated as conventional casted/forget metals since they do not exhibit any porosity like most of commercial sintered PM materials.

In a real HIP material at the PPBs several types of defects can be found, like unbonded surface, residual micro/nano-pores and inclusions (carbide, oxides): all these feature are constrained in a thin layer that can be described as a particulate reinforced MMC. Let us consider for simplicity the ideal case of a material fully densified and consolidated, in order to neglect the effect of other defect but nanoparticles.

A wide literature describes the action of inclusions in metals as brittle crack initiator, like in steels failing by cleavage [62-64], and as nucleation site for nano-voids growing by plastic deformation and coalescing up to the fracture [65-67]. Inclusions can crack or debond, depending on several factors, including the size, the mechanical behavior of the inclusions material, the interface strength and the stress and strain level experienced by the embedding matrix. Both in the case of cracking or debonding the inclusion fracture is described by a probability of failure based on a Weibull distribution derived by a weakest-ling model [64]:

$$P_f = 1 - exp[f(\sigma, \sigma_{cr}, \alpha)] \qquad \text{(IV.5)}$$

where σ is the tensile stress acting of on the particle, σ_{cr} is a critical stress determining the condition for failure and α is a set of parameters including also the size of the inclusions. Assuming a linear relationship between the matrix flow stress and the stress at the inclusion, Wallin [64] used a relation of the type for the cracking of carbides:

$$P_f = 1 - exp\left[-\left(\frac{d}{d_N}\right)^3 \left(\frac{\sigma^{matrix} - \sigma_{cr}^{matrix}}{\sigma_0}\right)^m\right] \qquad \text{(IV.6)}$$

where m and σ_0 are material dependent parameters, d is the inclusion diameter and d_N is a normalizing constant. The analysis of Walling demonstrated that the bigger the size the highest the probability of fracture. For inclusions of nanometric size the dominant failure mode is expected to be the debonding at the matrix-inclusion interface. This phenomenon can be described in term of a critical energy criterion [68] if the energy dissipated in debonding is expressed as:

$$W = U_d + U_m + U_p \qquad \text{(IV.7)}$$

where U_d represents the energy associated to the formation of the debonded surface ($U_d = 4\pi a^2 \gamma$ for a spherical inclusion of radius a and a cohesive surface energy γ); U_m and U_p represent the strain energy accumulated respectively by the matrix and by the inclusion. In metal matrix nano-composite the energy balancing enables to express the critical stress for debonding as [68]:

$$\sigma_{cr} = \left(\frac{\gamma}{a} \cdot \frac{4E_0}{1+\nu_0}\right)^{1/2} \qquad \text{(IV.8)}$$

The role of cohesive energy γ enlighten the fact that critical stress can be affected significantly by any factor raise or reduce γ, like for example the change in the chemistry of the interface due to the segregation of solute atoms. The segregation of hydrogen at the interface was claimed as a responsible of the lower-strength debonding of carbide as cause of brittle intergranular cleavage fracture. In [sabirov] the interface strength changes have been attributed to the aging heat treatment.

The analogy with MMC leads to consider several aspects like the volume of reinforcement and the matrix strength. The strength of the particle depends on the matrix strength according to a rule of the type $\sigma_{max}^{interf} = \sigma_{eq} + \sigma_m$ [60], with σ_{eq} equivalent stress and σ_m average stress in the medium. A stronger matrix reaches the critical stress for debonding at lower values of strain, so reducing the ductility of the composite. This effect takes place when a local cluster of inclusions [60,69] is present in a matrix: the matrix is strengthened just locally, so lower global load is needed to reach the critical stress. This is expected to be the case for samples with

a higher content of oxygen: a higher density of inclusions lowers the global load to determine the debonding. This interpretation is confirmed by the comparison of the load-deflection curves of the standard reference sample with the p4 sample already shown in fig. 13: this last sample nucleated the crack at appreciable lower load.

MMC fails by progressive damage accumulation during deformation by debonding/cracking of inclusions [61,68]. An example of damage accumulation in a HIPped N07627 is presented in fig. 23 a) where the SEM image of a longitudinal section of broken tensile sample is shown: the image reveals the formation of nano-voids along the PPBs; the coalescence of some nano-void formed a crack that advances along the PPB. The crack propagation in the same sample along a chain of precipitated is clearly imaged in the fig. 23 (b); the caption in the figure is a representative picture of the void-by-void mechanism of fracture.

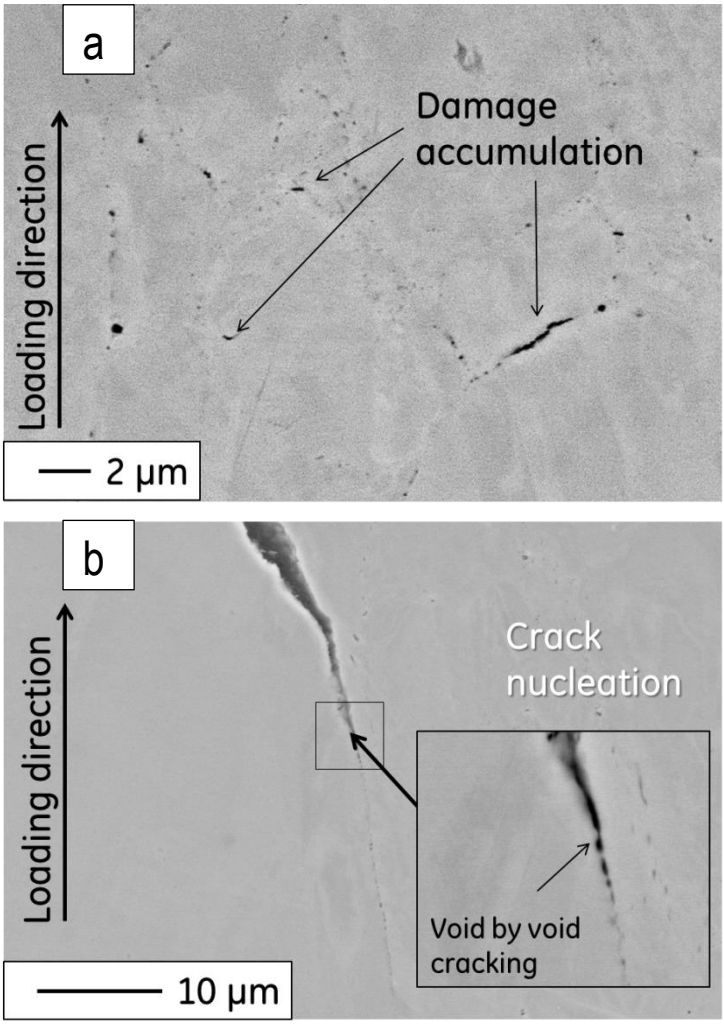

Fig. 23: SEM images of the longitudinal section of a loaded tensile specimen (ST-HIP, p2) : a) indication of damage accumulation by void formation at the PPBs; b) a particular of the crack nucleating and propagation along a PPBs, the microstructure of the crack front is shown at higher resolution in the caption.

4.4.3 - MMC model for fracture toughness

The PPBs then represent a preferential path for a propagating crack. Since the fracture advances by void by void nucleation at inclusions and coalescence, this system can be interpreted according the Ref. [62] that modeled by a Finite Element formulation the crack propagation in a visco-plastic material along a double array of spherical inclusions. In this case the fracture resistance Γ^0 is proportional to the mean spacing of the inclusions X_0 leading to a dependence of $(V_{inc})^{-1/3}$ [65]. At the critical value Γ^0 determining unstable crack propagation ($\Gamma^0 = J_{IC}$), i.e. the fracture toughness of the material, and assuming that the mean spacing is proportional the inverse of the cube of the voids nucleated at the inclusions (volume of de-bonded inclusions) V_{inc}, it is:

$$J_{IC} \propto \frac{1}{(V_{inc})^3} \propto \frac{1}{(c_{ox})^3} \qquad \text{(IV.8)}$$

A relation of this form was suggested also in Ref. [60] for MMC with mean diameter of reinforcement *d* and yield stress σ_Y, an exponent of -1/3 is used:

$$J_{IC} \propto \frac{\sigma_Y d}{(V_r)^{-1/3}} \qquad \text{(IV.9)}$$

In this case V_r represents the volume of reinforcement. This relation can be compared with the Charpy impact energy if a linear relation between the experimental J_{IC} and the Charpy impact energy is assumed as discussed in Ref. [70,71]. In order to validate such assumption the J_{IC} fracture toughness of several HIPped standard and non-standard N07626 samples processed with the same parameters and all the powder available (p1-p4 powders) with different intrinsic Charpy energy was measured: the results are reported normalized as function of charpy energy in fig. 24. The fit by linear relation presents several difficulties, related also to the effectiveness of the test with these materials. A detail worth of noting is that even if reference material exhibits good value of J at 0.2 mm offset of resistance curve, stable crack propagation is hard to reach in a test, so the results are pretty

indicative. Anyway at this stage of the knowledge of the material a linear relation is considered a reasonable approximation. So let us assume that the E_{CVN} Charpy energy can be related to the fracture toughness J_{IC} by:

$$E_{CVN} = \alpha J_{IC} + \beta \qquad \text{(IV.10)}$$

with α and β fitting coefficients.

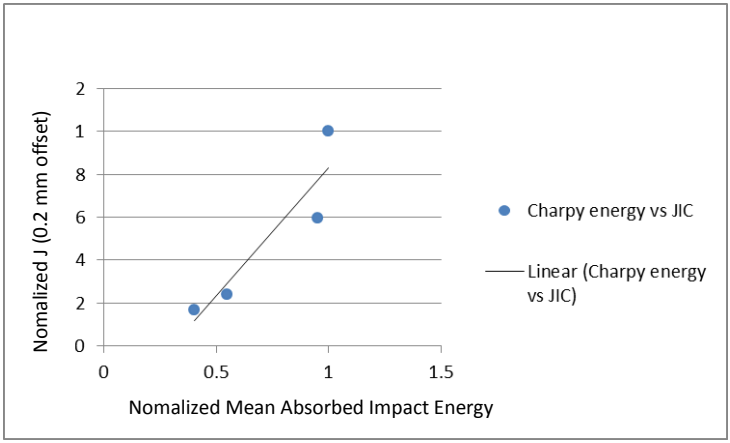

Fig. 24: J value measured at the 0.2mm offset as a function of mean absorbed impact energy measured in samples obtained from all powders (p1,p2,p3,p4) by the same ST-HIP processing.

So a correlation between the Charpy energy and the oxygen concentration is proposed combining eq. IV.8 and IV.10 and indicating with γ the proportionality coefficient between JIC and c_{ox}:

$$E_{CVN} = \alpha \frac{\gamma}{(c_{ox})^3} + \beta \qquad \text{(IV.11)}$$

The data of Charpy impact energy depending on oxygen concentration were fitted with a power low function of the type described in eq. IV.11; the model line is shown in fig. 25, suggesting a reasonable agreement. In this interpretation a

simplification assumption was done, i.e. that the dimension of inclusions is the same. In fig. 25 the MMC model is shown also with a dependence of $c_{ox}{}^{-1/3}$. The dependence with the inverse of the cube is characterized by a faster drop down of the fit curve, taking into accout the possibility that the volume of the inclusions is not due only to oxygen and the size of particle can be different. At this stage a reliable verification of the size distribution of the inclusions depending on oxygen concentration was not possible.

4.4.4 - *Analogy with DTB transition in steels: the Todinov model*

It has been shown that the fracture surface of the charpy specimens is partitioned in more ductile areas and smooth, quasi brittle zones. This fact suggests an interesting analogy with a very general discussion of the DTB transition in steels proposed in Ref. [72,73] depending on the absolute temperature on the system. The basic concept is that if just a small portion of the material is treated as brittle, and the fraction of such brittle domains is assumed decreasing monotonically as the temperature increases, the measured mean impact energy *E(T)* at the temperature *T* can be expressed according statistical consideration as:

$$E(T) = E_L + (E_U - E_L)(1 - exp[f(T)]) \qquad \text{(IV.12)}$$

where E_U and E_L represent the upper bound and the lower bound of the energy, *f(T)* is a not- decreasing function that can assumed a power law as:

$$f(T) = -k(T - T_0)^m \qquad \text{(IV.13)}$$

in which k and m are material properties and T_0 set the inset of the transition zone. An interesting aspect of the conclusion derived by Todinov is the volume fraction of the ductile regions V_d can be calculated by:

$$V_d = (1 - exp[-k(T - T_0)^m]) \qquad \text{(IV.14)}$$

A similar concept can be applied to PM material in relation with the oxygen content if it is assumed that the fraction of "brittle" domains in a P/M Ni-base superalloy grows monotonically with oxygen concentration c_{ox}. In this case an opposite behavior of the statistical function $f(c_{ox})$ has to be taken into account; this leads to a negative value of the parameter k. An example of the interpretation of the DTB transition data of the PM material with this model is provided in fig. 25 . This model describes better the lower bound of the energy curve, while it shows some difficulties in representing the upper bound.

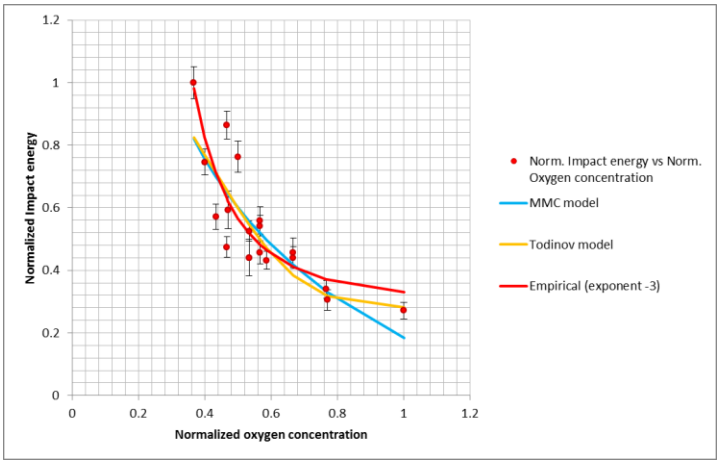

Fig. 25: Absorbed Impact energy over the oxygen concentration of samples processed according ST-HIP parameters by p1 powders: the interpolation of data by the MMC model and the Todinov model are included. The empirical fit with dependence of $c_{ox}{}^{-1/3}$ is also shown.

4.4.5 - *Intergranular fracture in P/M Ni-base superalloys*

In the section 4.2 It was noted that the PPBs mostly coincide with GBs, so if the fracture surface of a HIPped material is mostly interparticle it is also mostly intergranular. The preferential fracture along these surfaces has been associated to the scatter of nanometric inclusions. Actually an aspect remains to be clarified that is the possible role of embrittling factors of the GBs not intrinsically related to the

inclusions. In this case a brief discussion is provided of the main factor causing intergranular fracture in Ni-alloys.

In Ni-base alloys several mechanisms have been found leading to the transition from ductile-transgranular to brittle intergranular fracture, including Hydrogen embrittlement [74-75] and oxygen-associated dynamic embrittlement [76]. The segregation of sulphur at the grain boundaries has produced a ductile-to-brittle transition in nominally pure polycrystalline nickel [77]. Hydrogen embrittlement has been explained as the result of three general mechanisms: the formation of brittle hydrides, the hydrogen-enhanced localized plasticity (or HELP) and GB decohesion. The latter mechanism is part of more general phenomena of GB embrittlement due to the segregation of impurities that affect the energy of separation of the boundary to form free surfaces. Ref. [78] showed that the variation of cohesive energy due to a solute ΔE_b can be expressed as

$$\Delta E_b = \Delta E_{bond} + \Delta E_{chem} + \Delta E_{size} \qquad \text{(IV.15)}$$

In a ductile material the work of separation in an opening crack is the result of the sum of the energy needed to create 2 free surfaces, also referred as reversible work of fracture γ_{int}, corresponding to the cohesive energy, and the plastic work of fracture [62]:

$$W_S = 2\gamma_{int} + w_p \qquad \text{(IV.16)}$$

The term w_p accounts for the most of the separation energy, even 10 times more that the cohesive energy. It has been found that the two contribute of energy are somehow related, so a reduction in cohesive energy impacts significantly the total work of separation w_p that usually scales with γ_{int},. For hydrogen-embrittlement of ferritic steels Ref. [62] used a relation of the type:

$$w_p = A(2\gamma_{int})^q \qquad \text{(IV.17)}$$

with q = 6 and A = 0.0216. Ref. [79] proposed a linear relationship between the reversible work of fracture and the plastic energy in predicting the intergranular fracture of tubular steels.

As already anticipated, even the exposition of Inconel 718 to gaseous oxygen was demonstrated to be the cause of a transition from ductile-transgranular to intergranular of the crack path at medium-high temperature. If the phenomenon is well documented experimentally, the physical interpretation is attributed to a mechanism similar to the segregation of sulfur at GBs, i.e. to the reduction of cohesive energy of GBs [76].

In the investigated HIP material the analysis of the possible accumulation of segregates at GBs/PPBs is missing and is considered a point for future investigations. An interesting point to be clarified is the possible accumulation of H_2 in GBs/PPBs due to the dissociation of the residual water molecules present in the closed capsule for the oxidation of the metal powder at high-temperature.

4.5 - Improving toughness by changing process parameters

So far the properties of material processed according to a standardized cycle have been discussed. In this section the perspectives of improvements of the toughness properties by changing process parameters are discussed.

An increase of the HIP pressure didn't produce any significant variation to the mechanical properties of the standard material, so the results are not shown. On the other hand the increase of both HIP and solution treatment temperature has proven to be effective in improving the toughness of the material at the cost of a slight decrease of strength. This behavior was investigated in relation with the microstructure. The goal of an optimization of material properties was also to limit the grain growth in order to keep the strength.

4.5.1 - Grain size analysis

The effect of an increased HIP and solution temperature on grain size distribution was characterized by investigated by the analysis of grain-size distribution using EBSD. The Inverse Pole Figure (IPF) maps of samples T1HT1, T1HT2, T2HT1 and T2HT2 are shown in fig. 26: different color indicate distinct

crystals. The Oxford Channel 5 software suite enables the automatic identification and labelling of a large number of grains (several thousands), the diameter d_i of the grain *i* is then calculated as an equivalent diameter $d_{e,i} = 2\sqrt{A_i/\pi}$, where A_i is the grain area expressed in μm^2. Due to the spread in the size distribution a simple arithmetic average is very sensitive to the high numeric fraction of fine grains that correspond to a much smaller volumic fraction of the material. So the equivalent-diameter $\bar{d}_e$ is calculated also as a weighted mean:

$$\bar{d}_e = \frac{\sum_i d_{e,i} A_i}{\sum_i A_i} \qquad \text{(IV.18)}$$

Following Ref. [80], excluding the contribution of a large fraction of twins in the representation of the grain mean size can lead to unrealistic results. So an effective grain size can be calculated according to the relation (IV.9)

$$D_{eff} = \frac{\bar{d}_e}{1+2K_t ln\left(\frac{\bar{d}_e}{d_0}\right)} \qquad \text{(IV.19)}$$

where K_t is a constant and d_0 is the maximum diameter at which no twin boundary can be found. In this investigation the value of: K_t = 0.2 and d_0 = 1 μm, as suggested by the *Pande et al.*[17] for crystalline Nickel. The histogram of the arithmetic mean, the weighted mean and the effective diameter are shown in fig. 8. The values are calculated by the elaboration of a 1 mm square surface area. Applying the exclusion criteria a global but not massive increase of grains size with the increase of both HIP temperature and solution annealing temperature is observed, with an effect of the same order of magnitude for each increment in processing temperature. The effect of increased temperatures is much less effective using the definition of effective diameter.

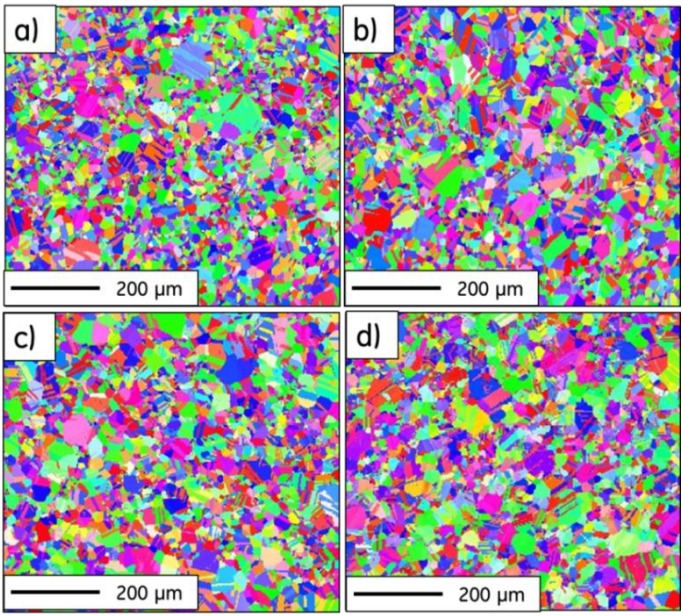

Fig. 26: Inverse Pole Figure maps of the samples processed according to the standard condition T1HT1 (a) and the experimental conditions T1HT2 (b), T2HT1 (c) and T2HT2 (d); for all samples the p1 powder was used (submitted in Ref. [37]) .

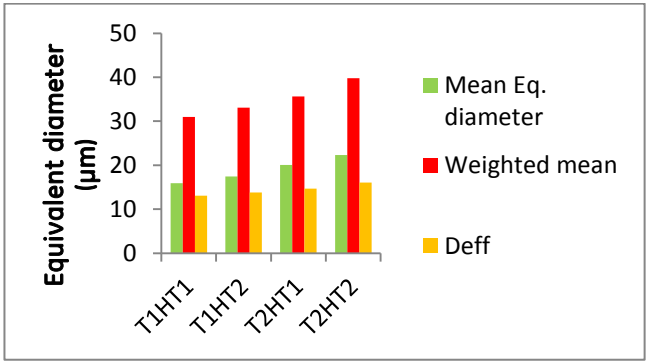

Fig. 27: Hystogram of the measured mean equivalent grain diameter of samples T1HT1, T1HT2 and T2HT2 calculated as an arithmetic mean (green), a weighted mean (red) and weighted mean with the correction for twins (orange). Picture submitted for publication in Ref. [37].

4.5.2 - Tensile properties

In fig. 28 a) the representative tensile stress-strain curves of the HIPped and Heat treated samples are shown: the curves are normalized. The increase in HIP temperature and/or the solution temperature leads to a slight decrease of the yield strength. The effect of the HIP and the solution temperature are of the same order of magnitude and substantially small. The most appreciable effect of increasing temperature is observed comparing the T1HT1 and T2HT2 samples with a decrease of the yield strength about 12.5 % in the T2HT2 sample. The relation between tensile properties and the average grain size suggests a strong sensitivity to mean grain size. This effect is observed also in the hardness of the material whose properties are not shown here. Even a limited grain growth can be anyway suitable to separate GBs from PPBs,

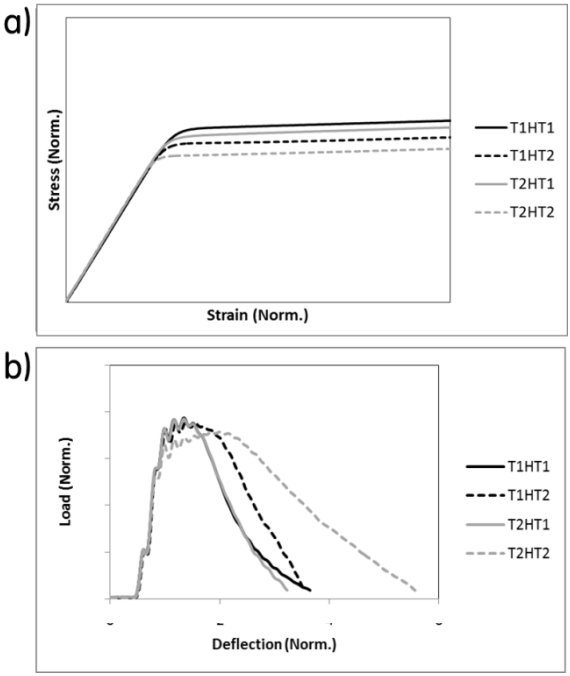

Fig. 28: a) normalized stress-strain curves of tensile samples T1HT1,T1HT2,T2HT1 and T2HT2; b) normalized load-deflection curves of Instrumented Charpy V-Notch specimens obtained by the same processing condition of (a). Submitted for publication in Ref. [37].

4.5.3 – Impact toughness

The effects of process parameter on load-deflection curves of the V-Notch Charpy tests are shown in fig. 28 b. The only increase of HIP temperatures doesn't affect the absorbed energy, represented by the area below the curves, while it leads to an appreciable improvement of impact toughness in the HT2 condition; furthermore a higher solution temperature improves the toughness of the samples hipped at the same temperature. These results could indicate that the effect of solution temperature can be larger regarding the impact toughness of the sample. The load at the onset of plastic yielding for sample T2HT2 is appreciably lower than the others, reflecting a drop in yield strength as indicated by tensile tests too. The

increase in absorbed energy is related to a widening of the yielding/crack nucleation portion of the curve].

4.5.4 -Interpretation of results

The key experimental results of the variation of process parameter and the identification of the constituent of the PPBs lead to the following considerations. PPBs constituents are strong oxides and carbides: these compounds are thermally stable at the processing temperature (dissolution temperatures of carbides is well above conditions selected (1200°C vs 1270°C reported in literature). Furthermore a slight grain growth is observed. These microstructural changes have a significant impact on mechanical properties by a slight softening of the matrix and by a significant improvement of the toughness.

Interpreting these results as related to the density of inclusions, in this case there is not variation of amount of oxygen and the carbides are supposed not to dissolve. So the explanation of a possible reduction of density of inclusions can be either a residual dissolution of oxides or a ripening. On the other hand the eq. IV.4 demonstrates that assuming the mass conservation of total volume of inclusions, their density can be reduced by the coarsening of the inclusions. In this case an Ostwald ripening can be supposed for the coalescence of oxides [81] and carbides [53,82]. The softening of the matrix was obserbed to increase the ductility of MMC [61], so ti can contribute to improve the toughness of the T2-HT2 material.

The last aspect to consider is the contribute of the separation of PPBs from GBs: it is thought to be effective in reducing the density of precipitate at the PPB, since the GBs are a preferential precipitation site for carbides as discussed in the metallurgy section at the beginning of the chapter.

The improvement in toughness of the T2HT2 samples is associated to an appreciable change in the appearance of the Charpy-specimen fracture surface compared to the reference ST-HIP material (i.e. T1HT1). A comparison in shown in fig. 29: the fig. 29a) and c) belong to a reference specimen (ST-HT, p1), and the fig. 29 b) and d) describe a T2HT2 sample (p1 powder). The latter exhibit globally much coarser dimples and the presence of smooth surfaces is reduced.

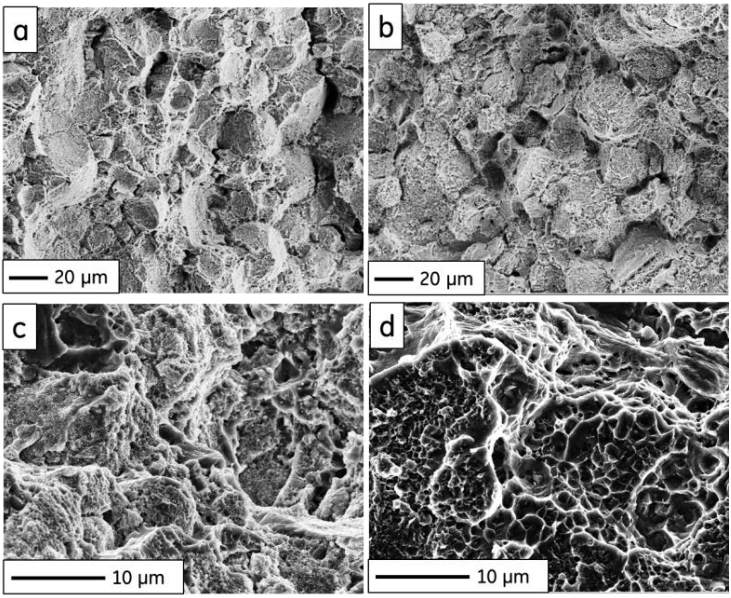

Fig. 29: SEM image of the fracture surface of broken Charpy V-Notch specimens processed to according T1HT1 condition a) and c); processed according tothe T2HT2 condition b) and d).

4.6 - Fatigue properties

4.6.1 – Fatigue in PM Ni-base superalloys: an overview

The fatigue properties of the PM ni-base alloys [83,84] have been widely investigated in last decades due to the criticality of the current main applications in term of design requirement. One of the most known and established application in turbomachineries is for alloy for aviation gas-turbine wheels, that are component subjected to heavy stress at relatively high temperature and to fatigue [85,86]. In these parts both low cycle fatigue [87,88] and high cycle fatigue [89] usually are

effective due to the cycle of start-up/shut-down of the machine and to the vibration of the wheels, respectively. Since the most advanced turbine-disk alloys are all based on powder metallurgy, a careful attention has been given to the intrinsic risk associated to the powder route.

The most studied topic concerns the analysis of the low cycle fatigue properties, in particular the aspect of the fatigue crack formation and early propagation. The powder processing route introduces a source of defect deriving from the atomizing technology of the metal powder itself [90]. These defects are constituted mainly by micrometric ceramic inclusions deriving from refractory materials abraded along the melt metal flow path in the inert gas atomizers, currently one of the most established production methods for Ni-alloys metal powder. The ceramic inclusions are usually screened in the sieving stage of the powder manufacturing, but smaller particles are still retained. In high strength Ni-base alloys operating at relatively high temperature, the density of ceramic inclusions is considered one of the limiting factor in the component life [83]. This fatigue aspect backed a strong effort in the elaboration of statistical models to describe the most critical locations of a stressed real part depending on the inclusion distribution and on the stress at the inclusions. In most of the models the inclusions are described as equivalent “short-crack” according to elasto-plastic models. The prediction of the life of the component depending on the inclusion size, the inclusion position, the stress and the characteristic crack-propagation law are essential for a reliable damage-tolerant approach [83] in design of turbine disks.

Due to the wide literature available on the topic, the description of the crack formation at ceramic inclusion will not be deepened in the following. Rather another aspect is interesting in an alloy like the N07626, prone to the formation of finely distributed nanometric precipitates at PPBs: the interaction of crack propagation with the PPBs and the relation with the toughness of the material. In order to investigate the interaction crack-PPBs fatigue crack growth rate tests were conducted on a standard material (good impact energy) and compared to the same test in sample that exhibited medium-low toughness and very low toughness.

4.6.2 – Fatigue Crack propagation in Ni-base superalloys

In conventional Ni-base alloys like forged Inconel 718, the fatigue crack propagation mode can be ideally divided in several stages depending on the intensity of the difference of stress intensity factor range ΔK as shown in fig. 30 adapted from Ref. [91] for a test ratio of R = 0.1 . As shown in the work of Mercer et al. the near-threshold stage and the lower Paris regime are characterized by the formation of thin striations and by a crack path preferentially driven by crystallography orientation. In this stage the propagation is usually considered poorly sensitive to the microstructure. In the upper Paris regime and the high ΔK stages, the crack propagation start to exhibit fracture mechanism similar to static loading; the fatigue striations transform progressively to ductile dimpling of a static fracture.

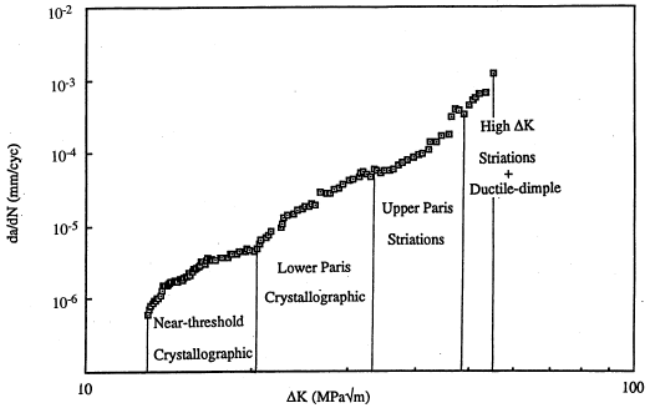

Fig. 30: Fatigue crack propagation curve of a forged sample of Inconel 718, adapted from Ref. [91].

4.6.3 – Fatigue Crack propagation in HIP N07626

In PM N07626 a similar behavior is found. In the near threshold and low Paris stage the crack propagation is insensitive of prior particle boundaries and proceed along crystallographic paths. An interesting aspect of this stage is that the crack crosses the PPBs without the significant nano-void formation and coalescence, giving a realistic image of an unbroken PPBs structure without plastic deformation. A representative image of this stage is provided in fig. 31 a) presenting the fracture

surface of a reference ST-HIP sample (powder p1): the crack front enlightened by the fatigue striations cuts a PPB separated by the closest GB; on the right side of the image a weakest PPB, aligned with the crack front, is encountered and opened.

The lower and upper Paris regime of fig. 30 are characterized in the PM alloy N07627 by a smooth transition from a “through-PPBs” to an “along-PPBs” propagation mode at the highest ΔK values. This phenomenon can be assumed as the general crack propagation behavior in this PM materials. The PPBs tends to be increasingly cracked at increasing stress intensity factor and the crack tends to follow the curved path of the PPBs at high ΔK. The fig. 31 b) shows the image of a cracked PPB where the striation formation is affected or even prevented where the nanometric precipitated are spread. The macroscopic appearance of the crack surface becomes fast very similar to the charpy fracture surface, presenting the rounded cavities and protrusions of the powder particle.

The global measure of the crack propagation rate of the three samples with different toughness is presented in fig. 32. These tests were conducted on samples processed according to ST-HIP parameter and using all the powder types: p1, p3 and p4. The material with the lowest toughness presents the less linear curve with a slope steeper than the tough material. The plastic response at high ΔK lead to two very different fracture mechanisms (see fig. 32) that is quasi-brittle for the less tough material and markedly ductile for the tough material. The toughness determines the propagation rate with a Paris slope (the m parameter) depending by the measured impact energy of the material by a linear relation as shown in fig. 33. One of the interesting results of this investigation that a linear relation can be found between the Charpy absorbed energy both with JIC and with the m Paris parameter.

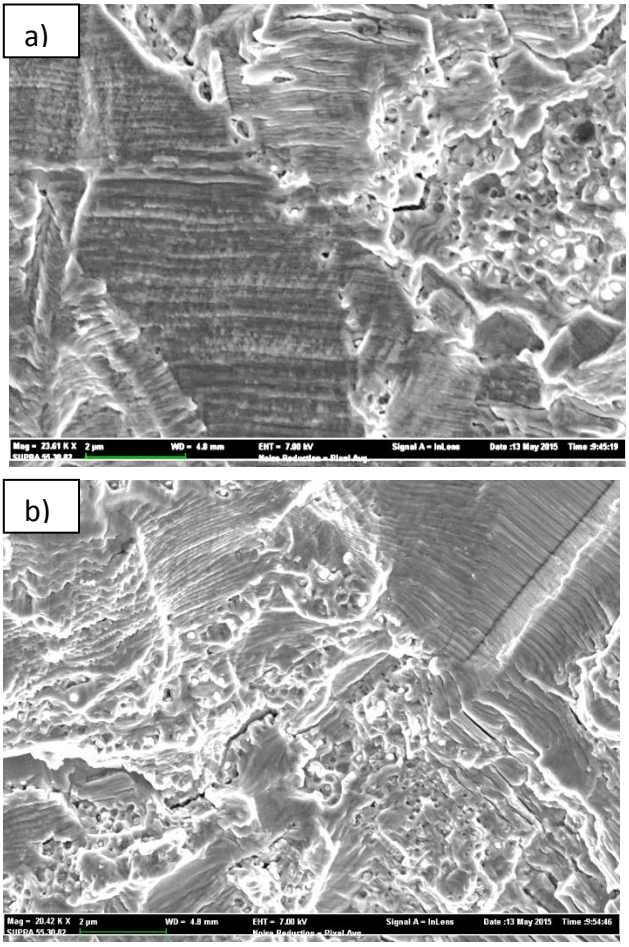

Fig. 31: a) SEM image of the fracture surface of a Fatigue Crack Propagation specimen sampled from HIP sample processed according to the standard ST-HIP parameters with powder p1, the image is taken in the zone of near-threshold stress intensity range; b) SEM image of fracture surface of the same specimen as above taken in the low Paris-Upper Paris transition regime.

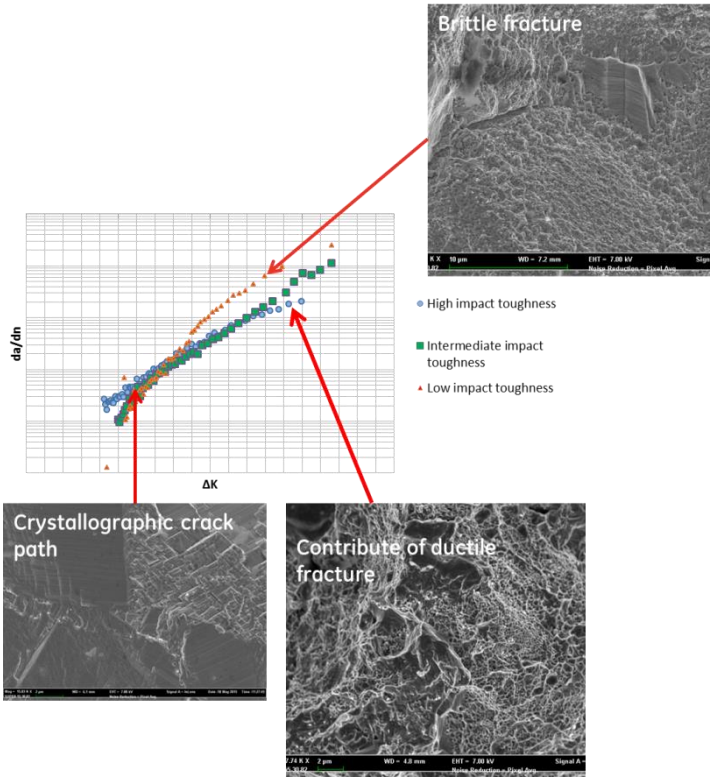

Fig. 32. Fatigue Crack Propagation curve of three samples produced according the to ST-HIP parameters with powder p1,p2 and p3, exhibiting respectively good toughness, low toughness and very low toughness. The SEM images show the fracture surface in the near-threshold and in the high- ΔK regime of the toughest and the less tough sample.

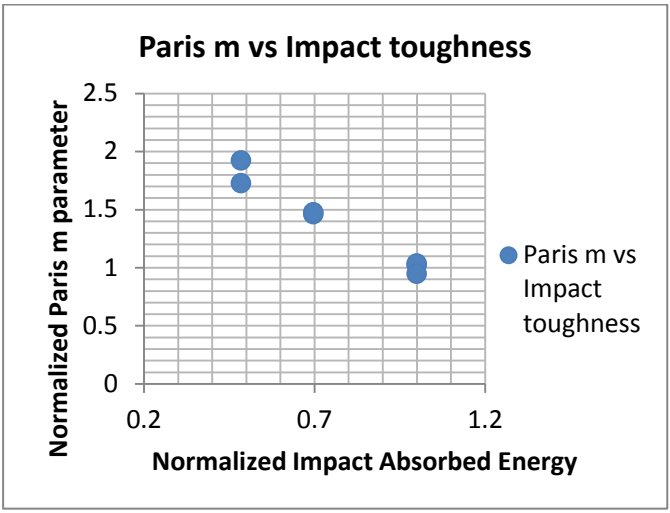

Fig. 33: Measured slope parameter of the Paris law in samples processed according to ST-HIP condition with powder p1, p2, p3 reported as function of the measured mean Impact absorbed energy.

Chapter V

Conclusions and future perspectives

This thesis presented a selection the most relevant results of a research activity conducted in collaboration with the *Material and Processes Engineering* Department of *General Electric Oil & Gas* (Italy) for the investigation of the applicability of powder metallurgy (P/M) technologies to the manufacturing of turbomachineries' components. The research activity analyzed two P/M technologies and several materials. This work is focused just on a single processing technology, Hot Isostatic Pressing, and a single material, the corrosion resistant Ni-base alloy N07626.

The densification behaviour of the N07626 metal powder in condition of pressure assisted sintering was investigated by experiments conducted on a small scale by uniaxial hot pressing condition using a Spark Plasma Sintering machine at least in the initial stage of densification. The sintering conditions were comparable with a full scale HIP commercial process, indicating that in the pressure and temperature conditions applied the effect of pressure variation impacts much less the densification rate than a small variation of sintering temperature. This behaviour depends on the strong contribution given by diffusive mechanisms that are temperature activated. The work proposed to extend these results to a full scale HIP process, supporting the interpretation that diffusional creep mechanisms can be dominant in the early densification stage of Ni-superalloys and suggesting that an increment of pressure in a HIP cycle could lead just a small enhancing of densification, while a small increment in temperature raises up the compaction rate.

The work then presented the results of the microstructure and mechanical properties of full-dense HIPped samples and full-scale parts of N07626 alloy, produced according to a fixed proprietary cycle, to investigate the variability and repeatability of the properties, and several experimental deviations from this baseline in order to investigate the effect of process parameters for perspectives of future improvements. The microstructural analysis was conducted by several analytical techniques, including Optical Metallography, Scanning Electron Microscopy, Energy Dispersed X-Ray Spectroscopy and Electron Backscatter Diffraction. The

mechanical properties of the alloy were assessed by tensile testing, conventional and instrumented Charpy V-Notch testing, J_{IC} fracture toughness tests and fatigue crack propagation rate testing.

The statistical evaluation of the tensile and Charpy properties of the material processed according a reference processing cycle provided the following main results:

1) the tensile properties are impacted by localized accumulation of oxygen in the consolidated part in so called Oxygen Affected Zones (OAZs);

2) the mean yield strength is not sensitive to oxygen accumulation, while both the mean tensile ductility and mostly the mean impact toughness are dramatically impacted by such an accumulation;

3) the accumulation of oxygen leads to a ductile to brittle transition in the impact toughness of the material.

4) the fracture occurs preferentially along the prior particle boundaries and the fracture mode is tightly related to the dense clustering of nano-inclusions in a thin layer along the PPBs, associated to micro-ductility phenomena by void nucleation and coalescence.

The accumulation of oxygen in the OAZs and the formation of nano-inclusions at the PPBs were interpreted discussing the phase transformations of the metal oxides present on the surface of the metal powder and all foreign oxides in the global closed system represented by a consolidating HIP capsule. Discussing such transformations in analogy with the phenomena of solid-state diffusion bonding, the nano-inclusions were interpreted as the result of agglomeration of oxides, precipitation of novel oxides and MC high-solvus carbides. The OAZs were explained by two possible mechanisms: the diffusion of oxygen from destabilized oxides to Ni-base powder and desorption of entrapped moisture with the preferential oxidation of hottest zone of the system, formed due the reasonable strong temperature gradient inside the capsule.

The fracture mode of the PM alloy was interpreted as a process of micro-ductility by damage accumulation and crack propagation by inclusions debonding/cracking along the PPBs, following an analogy with: 1) models of ductile fracture by void-by-void nucleation and coalescence; 2) the behaviour of

particulate-reinforced metal-matrix composites (MMC) that were thought able to represent the thin layer of inclusions. This analogy provided a model to explain the DTB transition on the base of the density of inclusions by relating the impact toughness of the material to inverse of the cube of the oxygen concentration. The DTB transition was further discussed in term of a general statistical model derived from the temperature-dependent DTB transition in steels.

The fatigue crack propagation of the reference material was then investigated and compared with experimental samples of material characterized by increasingly poorer impact toughness properties. In agreement with a Paris-like crack propagation in forged Ni-base alloys, the crack propagation in the P/M material was insensitive of the PPBs nano-inclusions in the near-threshold regime, while a progressive transition from crystallographic to inclusion-mediated crack path took place in the intermediated Paris regime. In the high stress intensity range stage the different toughness leads to very different propagation rate. The slope parameter of the Paris relation was found approximately proportional to the mean representative impact toughness of the samples.

The effect of HIP parameters deviation from reference was finally investigated. The application of increased HIP and solution annealing temperature proved to be appreciably beneficial for the toughness of the material, leading to a concomitant slight softening of the strength. This effect was related to the grain structure enlightening that the change in mechanical properties corresponded to a very moderate grain growth. These results were interpreted on the base of the density of precipitates at the PPBs. The process temperatures applied were considered too low for a complete dissolution of these nano-inclusions, so the novel toughness properties are related to the possible ripening of the precipitates, the separation of grain boundaries from PPBs and to the softening of the matrix. This last result is promising since it has been demonstrated that even sub-solvus heat treatment can result beneficial for mechanical properties of N07626, with a limited grain growth, instead of super-solvus treatment proposed by other authors.

The research activity requires a closer examination of several open points. The DTB transition in impact toughness was measured in several parts: a more controlled measurement of both the oxygen content and the relative

mechanical properties is whished in order to consolidate the statistics and the representativeness of the data. The surface chemistry of the particle surface of the N07626 powder was not analyzed directly prior the HIP consolidation, so further investigations should focus on this topic. In particular the factors of weakening of intergranular cohesion, i.e. intergranular solute segregation, should be clarified. The fracture toughness assessment of the samples must be consolidated by a wider test campaign in order to find a more reliable relation with the Charpy impact toughness. Furthermore a more accurate measurement of the inclusion density and morphology is considered important, and the application of further Electron Microscopy techniques must be considered in order to consolidate the interpretation provided in this work.

VI - Appendix

6.1 - Novel perspectives of applications of Powder Metallurgy technologies for Oil & Gas turbomachineries

Powder Metallurgy technologies have proven to be effective and beneficial also for the manufacturing of a variety of metal alloys that can be applied in the Oil & Gas turbomachineries. The aim of this short appendix is to show the perspectives of application of:

1) Hot Isostatic Pressing to the processing of titanium alloys;
2) Additive manufacturing by Selective laser Melting of Ni-base superalloys.

This chapter reports also part of the results produced in the collaboration with GE Oil & Gas in the course of PhD that were not discussed in the body of the thesis.

A.1 - HIP of Titanium alloys

The titanium alloys represents materials of great interest for applications in O&G turbomachineries for the combination of extraordinary mechanical properties and a notable corrosion resistance [92,93]. The essential mechanical characteristic of Ti alloys is the high specific strength associated to a low density, making them ideal for applications in which a reduction of weight is determinant. The fig. 1 shows schematically the field of industrial application of Ti alloys with other categories of metal alloys in term of high specific strength and operating temperature.

The titanium alloys can exhibit a variety of phase structures basically divided in three categories: 1) a hexagonal closed packed structure called α-phase, 2) a body centered cubic phase called β phase or 3) the stability of both previous phases in the α+β structure. The pure titanium at room temperature has an α structure, the β phase becomes stable at high temperaure above a value known as β-transus. A proper alloying of the titanium makes stable also β at low temperature: this is the basis of the development of the α+β and β alloys. Furthermore the balance of the relative amount of α and β makes possible a great variety of mechanical behavior.

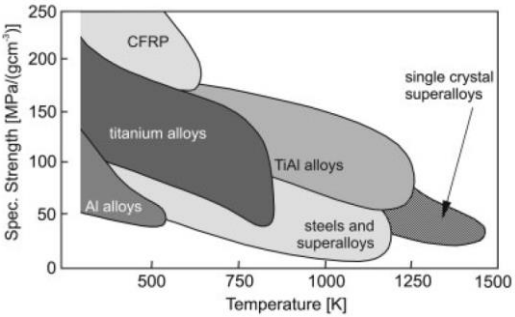

Fig. 1: a diagram representing the industrial field of application of titanium alloys depending on specific strength and operating temperature compared with other metallic alloys.

The application of HIP to titanium alloys have been investigated by many authors [4,94,95], in particular regarding the advantages of HIP Net-Shape manufacturing as demonstrated in Ref. [4,5]. The fig. 2 shows a part produced by an advanced P/M Net shape processing adapted from Ref. [5]: the picture shows an impeller made by Ti6Al4V for applications in liquid hydrogen and demonstrate clearly the shape complexity that is demanded to a Net-Shape HIP manufacturing.

In the course of the PhD research activity a preliminary investigation of the metallurgy and of the mechanical properties of the HIPped Ti alloy Ti-6Al-2Sn-4Zr-6Mo was started. Some of the most relevant results were published in Ref. [96]. The Ti-6Al-2Sn-4Zr-6Mo alloy is a high strength titanium alloys, exhibiting relatively high toughness, whose microstructure and properties are determined by dedicated heat treatments of solutioning and aging. The characteristic microstructure resulting by several heat treatments above and below the β transus was investigated in detail, with attention also to the cooling rate. In the case of fast cooling from above a sort of critical temperature, just below the β transus, a martensitic α″ structure formed. A valid result of the study was the analysis of the X-Ray diffraction spectrum for a quantitative measurement of the amount of the phases. The correlation of the microstructure with the mechanical properties was achieved by microhardness testing, showing that the hardness is linearly proportional to the fraction of the finely transformed β phase stable after aging. Further investigation should focus on the optimization of the toughness and ductility of the material and the sensitivity of the

material to the embrittlement by the accumulation of dissolved oxygen has to be clarified.

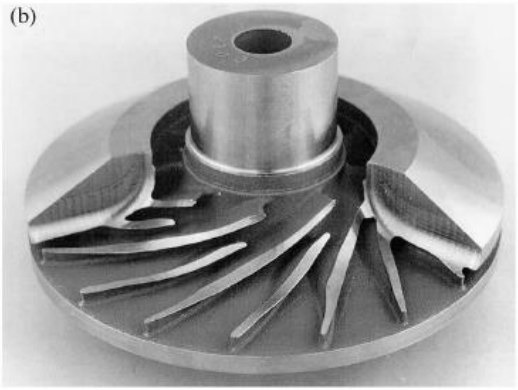

Fig 2: HIPped impeller made by Ti-6Al-4V alloy reported as example of net-shape manufacturing in Ref. [5].

A.2 - Additive manufacturingof Ni-base superalloys

The additive manufacturing of metal bodies has established as a disruptive group of technologies in recent years, with the ambition of changing dramatically the conventional production processes [97,98]. It has been applied to a variety of metals and alloys, including Ni-base superalloys currently used in Oil & Gas Turbomachinery [99,100]. Among the additive manufacturing technologies, in this appendix the Selective Laser Melting is mentioned. It is based on a precise melting of metal powder by a laser beam; the process is repeated in many layers of melting in order to build a 3-dimensional body [101].

As representative example of Ni-base alloy processed by SLM it is cited a detailed investigation of the microstructure and mechanical properties of SLM processed Inconel 718 in Ref. [99]. This work is usefull to introduce the novel metallurgical aspects associated to the introduction of this P/M technology. The SLM materials exhibit a characteristic microstructure with strong anisotropy resulting by the melting layer by layer. This microstructural anisotropy is associated also to a concomitant anisotropy of mechanical properties.

The optimization of high temperature homogenization of SLM Inconel 718 was investigated in the PhD activities and part of the results was published in Ref. [102]. The application of the Electron Backscatter Diffraction was very useful in characterizing the novel microstructure and in guiding in a quantitative interpretation of the heat treatment effectiveness. A typical as-built microstructure is presented in fig. 3a) in Inverse Pole Figure maps, the analyzed sample presents extremely different structure along the growth direction Z (left) and in the growth plane XY (right). It is interesting compare this columnar structure with the homogenized one showed in fig 3b).

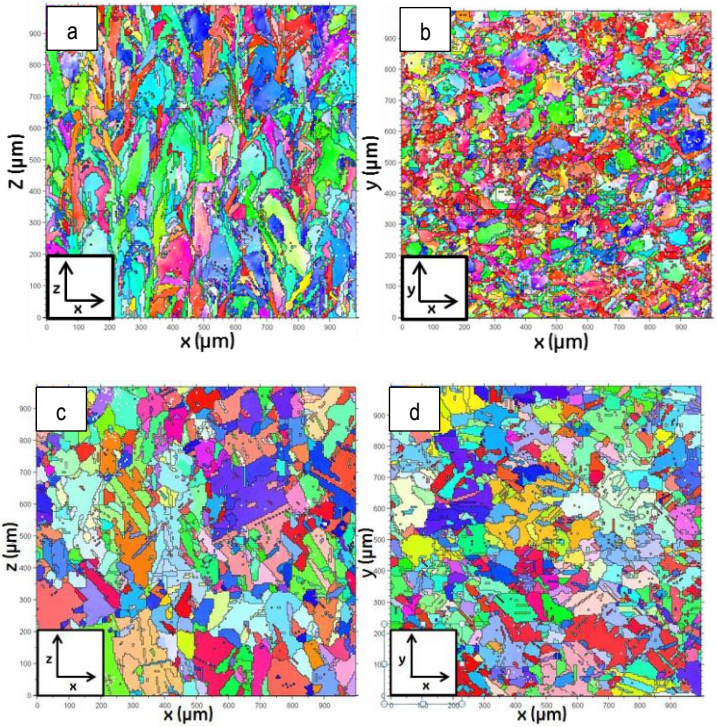

Fig. 3: EBSD Inverse Pole Figure maps of two sample of Inconel 718 produced by Selective Laser Melting adapted from Ref. [102]: a) as-build condition in the plane XZ orthogonal to the deposition plane (XY); b) as-build condition in the plane XY; c) homogenized sample in in the plane XZ; d) homogenized sample in in the plane XZ.

The advantages provided by the EBSD analysis consist in the possibility to characterize the gradient of intra-granular misorientation, a sort of measure of how much the crystals are distorted by the thermal stress and rapid solidification processes. This parameter can be compared after a conventional heat treatment and a homogenization to assess the effect of the process.

The novel challenges for researcher are not limited just to the anisotropy of the microstructure. The behavior of the 17-4 PH stainless steel represents an exemplar case of metallurgical properties still to clarify [103]: despite of the name (PH stands

for precipitation hardening) the 17-4 PH processed by SLM doesn't exhibit a regular precipitation hardening[, and the reason is still unexplained.

VII - References

[1] H.V. Atkinson and S. Davies - Metallurgical and Materials Transactions A, vol. 31a, pp 2981-3000 (2000);

[2] Sintering: From Empirical Observations to Scientific Principles; Randall German, 2014 Elsevier Inc.

[3] M.A. Ashworth, M.H.Jacobs, S. Davies, Materials & Design, vol. 21, p. 351-358 (2000);

[4] W.X. Yuan, J.Mei, V. Samarov, D. Seliverstov, X.Wu; Journal of Materials Processing Technology, vol. 182, pp. 39–49 (2007);

[5] R. Baccino, F. Moreta , F. Pellerin, D. Guichard, G. Raissond, Materials and Design, vol. 21, pp. 345-350 (2000);

[6] G. Masi, P. Stella, M. Giannozzi, F. Iozzelli, *"Perspectives Of The Application Of High Strength Nickel Base Alloys by Hip in Rotating Equipment For Oil & Gas Industry"* in HIP '14 - 11° International conference of Hot Isostatic Pressing, Stockholm 9-13 June 2014;

[7] *"Sintering theory and practice",* R.German, Wiley-Interscience, New York, US (1996);

[8] *"Sintering. Densification, GrainGrowth and Microstructure";* Suk-Joong L. Kang; Elsevier Butterworth-Heinemann, Linacre House, Jordan Hill, Oxford (2005);

[9] E. Artz. M.F. Ashby, K.E. Easterling, Metallurgical And Materials Transactions A, vol 14A, pp 211-221 (1983);

[10] A.S. Helle, K.E.Easterling, M.F. Ashby, Acta metallurgica, Vol 33, pp 2163-2717 (1985);

[11] *"Nickel, Cobalt, and Their Alloys"*, J. R. Davis, Davis & Associates, 2000 ASM International, Materials Park, OH 44073;

[12] Reference Module in Materials Science and Materials Engineering, from Comprehensive Structural Integrity, V.S. Srinivasan, A. Saxena, vol. 5, pp. 374-403 (2007);

[13] Cyprien Wolff, Sébastien Mercier, Hervé Couque, Alain Molinari, Mechanics of Materials, vol. 49 , pp. 72–91 (2012);

[14] H. ElRakayby, H.Kim b, S. Hong, K. Kim, Advanced Powder Technology, vol. 26, pp. 1314–1318 (2015);

[15] Christian Geindreau, Didier Bouvard, Pierre Doremus, Eur. J. Mech. A/Solids, vol. 18, pp. 581–596 (1999);

[16] Y. Takahashi, T.Nakamura, T. Nishiguchi, Journal of Materials Science, vol. 27, pp. 485-498 (1992);

[17] Z. A. Munir, Journal of Materials Science, vol. 14, pp. 2733-2740 (1979);

[18] Y. Maheara, Y. Komizo, T.G. Langdon, Materials Science and Technology, vol. 4, pp. 669-674 (1988);

[19] W.W. Basuki, O. Kraft, J. Aktaa, Materials Science and Engineering A, vol 538, pp. 340-348 (2012);

[20] A.A. Shirzadi, H. Assadi, E.R. Wallach, Surface and Interface Analysis, vol. 31, pp. 609-618 (2001);

[21] J.J. Debarbadillo and S. K. Mannan, JOM, vol. 64, pp. 265-270 (2012);

[22] Z. A. Munir, D. V. Quach, M. Ohyanagi, Journal of the American Ceramic Society, vol. 94, pp. 1-19 (2011);

[23] Z. A. Munir, U. Anselmi-Tamburini, M. Ohyanagi, Journal of Materials Science, vol. 41, pp. 763-777 (2006);

[24] U. Anselmi-Tamburini, J.E. Garay, Z. a. Munir, Materials Science and Engineering A, vol. 407, pp. 24-30 (2005).

[25] W. Chen, U. Anselmi-Tamburini, J.E. Garay, J.R. Groza, Z. a. Munir, Materials Science and Engineering: A, vol. 394, pp. 132-138 (2005);

[26] R. Orrù, R. Licheri, A.M. Locci, A. Cincotti, G. Cao, Materials Science and Engineering: R: Reports, vol. 63, p. 127-287 (2009);

[27] ASTM E8 / E8M-15a, *"Standard Test Methods for Tension Testing of Metallic Materials",* ASTM International, West Conshohocken, PA, 2015;

[28] ASTM E23-07a, *"Standard Test Methods for Notched Bar Impact Testing of Metallic Materials*", ASTM International, West Conshohocken, PA, 2007;

[29] "*Fracture Mechanics: Fundamentals and Applications"*, Ted L. Anderson, CRC Press LLC, Boca Raton, FL, US (1995);

[30] ASTM E1820-08a, *"Standard Test Method for Measurement of Fracture Toughness"*, ASTM International, West Conshohocken, PA, 2008;

[31] ASTM E647-11, *"Standard Test Method for Measurement of Fatigue Crack Growth Rates"*, ASTM International, West Conshohocken, PA, 2011;

[32] Angus J. Wilkinson and T. Ben. Britton, Materials Today, vol. 15, pp. 366-376 (2012);

[33] *"Electron Backscater Diffraction in Material Science",* A. J. Schwartz · M. Kumar, B. L. Adams, D. P. Field, Springer Science+Business Media, LLC, New York, NY,US (2009);

[34] P. Stella, M. Buccioni, A. Molinari, "*Spark Plasma Sintering of a nickel-base superalloy*", Proceedings EURO PM2013 Congress & Exhibition, Gotheborg 15-18 September 2013, ed. EPMA, Shrewsbury (UK), vol. 1, pp. 421-426;

[35] E.G. Grigoryev, E.A. Olevsky, Scripta Materialia, vol. 66, pp. 662-665 (2012);

[36] D.M. Hulbert, A. Anders, J. Andersson, E.J. Lavernia, A.K. Mukherjee, Scripta Materialia, vol. 60 , p. 835-838 (2009);

[37] P. Stella, G. Masi, A. Molinari, "*Microstructure and mechanical properties of the P/M precipitation-hardening alloy N07626: effect of HIP temperature and solution annealing*.", submitted to Powder Metallurgy;

[38] L. Chang, W. Sun, Y. Cui, R. Yang, Materials Science & Engineering A, vol. 599, pp. 186–195 (2014);

[39] L. Chang, W. Sun, Y. Cui,F. Zhang, R. Yang, Journal of Alloys and Compounds, vol. 590, pp. 227–232 (2014);

[40] G.A Rao, M. Kumar, M. Srinivas, D.S.Sarma, Materials Science & Engineering A, vol. 355, pp. 114-125 (2003);

[41] H. L. Eiselstein and D. J. Tillack in E. A. Loria (editor), *Superalloys 718, 625 and Various Derivatives*; Warrendale, PA: TMS, (1991);

[42] V. Shankar, K.B.S. Rao, S.L. Mannan; Journal of Nuclear Materials, vol. 288, pp. 222-232 (2001);

[43] W.D. Cao, R.L. Kennedy, M.P. Willis in E.A. Loria (Editor), *Superalloys 718, 625 and Various Derivatives*, Warrendale, PA: TMS, (1991).

[44] G. Xie, O. Ohashi, M. Song, K. Furuya and T. Noda, Materials Science & Engineering A, vol 34A, pp. 699-703 (2003);

[45] D. Chasoglou, E. Hryha, L. Nyborg, Materials Chemistry and Physics, vol. 138, pp. 405-415 (2013);

[46] H. Danninger, C. Gierl, S. Kremel, G. Leitner, K. Jaenicke-Roessler, Y. Yu, Powder Metallurgy Progresses, vol. 2, pp. 125-140 (2002);

[47] *"Introduction to the High Temperature Oxidation of Metals"*, Neil Birks, Gerald H. Meier, Frederick S. Pettit, Cambridge University Press, The Edinburgh Building, Cambridge UK (2009);

[48] N. Birks, G.H. Meier, and F.S. Pettit, JOM, vol. 46, pp. 42-46 (1994);

[49] S.Özbilen, A. Ünal and T.Sheppard, Oxidation of Metals, vol. 53, pp. 1-23 (2000);

[50] M. Kumar, T.V. Balasubramanian, R.D.K. Misra, Journal of Material Science Letters, vol. 9, pp. 147-151 (1990);

[51] L. Kumar, R. Venkataramani, M. Sundararaman, P. Mukhopadhyay and S. P. Garg, Oxidation of Metals, vol. 45, pp. 221-224 (1996).

[52] J. P. Neumann, T. Zhong and Y. A. Chang, Bulletin of Alloy Phase Diagrams, vol. 5 No. 2 (1984);

[53] N.G.Ingesten, R. Warren, L. Winberg in R. Brunetaud et al. (eds.) in *"High Temperature Alloys for Gas Turbines"*, ECSC, EEC, EAEC, Brussels and Luxembourg (1982);

[54] G. Appa Rao, M. Srinivas a, D.S. Sarma, Materials Science and Engineering A, vol. 435–436, pp. 84–99 (2006);

[55] R. Waters, J.A. Charles, C. Lea; Metals Technology, vol. 8, pp. 194-200 (1981);

[56] G. Appa Rao, M. Srinivasa, D.S. Sarma, Materials Science and Engineering: A, vol. 418, pp. 282–291 (2006);

[57] L.G. Zhao, Journal of Engineering Materials and Technology, vol. 33, pp. 031002-1-7 (2011);

[58] M. Yamasaki and Y. Kawamura, Materials Transactions, vol. 47, pp. 1902-1905, (2006);

[59] A. V. Gusarov, P. Kovalev, Physical Review B, vol. 80, pp. 024202-1-15 (2009);

[60] I. Sabirov, O. Kolednik, Materials Science and Engineering A, vol. 527, pp. 3100–3110 (2010);

[61] A. Hauert, A. Rossoll, A. Mortensen, Journal of the Mechanics and Physics of Solids, vol. 57, pp. 473–499 (2009);

[62] P. Novak, R.Yuan, B.P.Somerday, P.Sofronis, R.O.Ritchie, Journal of the Mechanics and Physics of Solids, vol. 58, pp. 206–226 (2010);

[63] S.R. Bordet, A.D. Karstensen, D.M. Knowles, C.S. Wiesner, Engineering Fracture Mechanics,vol. 72 pp. 435–452 (2005);

[64] K. Wallin, T. Saario, and K. Törrönen, Metal Science, vol. 18, pp. 13-16 (1984);

[65] V. Tvergaard, J. W. Hutchinson, International Journal of Solids and Structures, vol. 39, pp. 3581–3597 (2002);

[66] A. Srivastava, L. Ponson, S. Osovski, E. Bouchaud, V. Tvergaard, A. Needleman, Journal of the Mechanics and Physics of Solids, vol. 63, pp. 62–79 (2014);

[67] V. Tvergaard, J.W. Hutchinson, Journal of the Mechanics and Physics of Solids, vol. 40, pp. 1377-1397 (1992);

[68] J. N. Dastgerdi, G. Marquis, M. Salimi; Composites Science and Technology, vol. 93, pp. 38–45 (2014);

[69] I. Sabirov, O. Kolednik, R.Z. Valiev, R. Pippan; Acta Materialia, vol. 53, pp. 4919–4930 (2005);

[70] J.R. Tarpani and D. Spinelli, Material Science and Technology, vol. 19, pp. 1435-1441 (2003);

[71] K. Wallin, Fatigue Fracture Engineering Materials Structures, vol. 24, pp. 537-549 (2001);

[72] M.T. Todinov, Materials Science and Engineering A, vol. 265, pp. 1–6 (1999);

[73] M.T. Todinov, M. Novovic, P. Bowen, J.F. Knott, Materials Science and Engineering A, vol. 287, pp. 116–124 (2000);

[74] M.L. Martin, B.P. Somerday, R.O. Ritchie, P. Sofronis, I.M. Robertson; Acta Materialia, vol. 60, pp. 2739–2745 (2012);

[75] M. Q. Chandler, M.F. Horstemeyer, M.I. Baskes, G.J. Wagner, P.M. Gullett, B. Jelinek; Acta Materialia, vol. 56, pp. 619-631 (2008);

[76] U. Krupp, W.M. Kane, C. Laird, C.J. McMahon, Materials Science & Engineering A, vol. 387-389, pp. 409-413 (2004);

[77] S. Mahalingam, P.E.J. Flewitt, J.F.Knott; Materials Science & Engineering A, vol. 564, pp. 342–350 (2013);

[78] M. Gibson, C. A. Schuh, Scripta Materialia, vol. 113, pp. 55-58 (2016);

[79] L.J. Qiao, W.Y. Chu, J.L. Luo, Materials Science and Engineering A, vol. 276, pp. 141-146 (2000);

[80] C.S. Pande, B.B. Rath, M.A. Imam, Materials Science and Engineering A, vol. 367, pp. 171–175 (2004);

[81] D. Srinivasan, P.R. Subramanian, Metallurgical and Materials Transactions A, vol. 37, pp 3455-3468 (2006);

[82] A. Mitchell, A.J. Schmalz, C. Schvezov and S.L. Cockcroft, in E.A. Loria (editor) Superalloys 718, 625,706 and Various Derivatives, TMS, (1994);

[83] *"The Superalloys, Fundamentals and Applications"*, R.C. Reed, Cambridge University Press, The Edinburgh Building, Cambridge UK (2008);

[84] Andre Pineau, Stephen D. Antolovich, Engineering Failure Analysis, vol. 16, pp. 2668–2697 (2009);

[85] G. Raisson , Powder Metallurgy, vol. 51, pp.10-13 (2008);

[86] D. Furrer and H. Fecht, vol. 51, pp. 14-17 (1999);

[87] K. O. Findley and A. Saxena, Metallurgical And Materials Transactions volume 37a, pp. 1469-1475 (2006);

[88] J. Luo, P. Bowen, Acta Materialia, vol. 51, pp. 3521–3535 (2003);

[89] A. Shyam, S.A. Padula, S.I. Marras and W.W. Milligan, Metallurgical and Materials Transactions A Volume 33a, pp. 1949 (2002);

[90] J. Grison And L. Remy, Engineering Fracture Mechanisc, vol. 57, pp. 41-55 (1997);

[91] C. Mercer, A.B.O. Soboyejo, W.O. Soboyejo; Materials Science and Engineering A, vol. 270, pp. 308–322 (1999);

[92] *"Titanium and Titanium Alloys"*, C. Leyens and M. Peters (editors), Wiley-VCH Verlag GmbH & Co KGaA, Weinheim (2003);

[93] M. Peters, J. Kumpfert, C.H. Ward, C. Leyens, Advanced Engineering Materials, vol. 5, pp. 419-427 (2003);

[94] D.P. Delo, H.R. Piehler, Acta Materialia, vol. 47, pp. 2841-2852 (1999);

[95] K. Zhang, J. Mei, N. Wain, X. Wu; Metallurgical and Materials Transactions A, vol. 41A, pp. 1033-1045 (2010);

[96] P. Stella, I. Giovanetti, G. Masi, M. Leoni, A. Molinari; Journal of Alloys and Compounds, vol. 567, pp.134–140 (2013);

[97] D. D. Gu, W. Meiners, K. Wissenbach and R. Poprawe, International Materials Reviews, vol. 57, pp. 133-164 (2012);

[98] S. Das, M. Wohlert, J. J. Beaman, D. L. Bourell, JOM, vol. 50, pp. 17-20 (1998);

[99] K.N. Amato, S.M. Gaytan, L.E. Murr, E. Martinez, P.W. Shindo,

J. Hernandez, S. Collins, F. Medina; Acta Materialia, vol. 60, pp. 2229–2239 (2012);

[100] P. Ganesha, R. Kaul, C.P. Paul, Pragya Tiwari, S.K. Rai, R.C. Prasad, L.M. Kukreja; Materials Science and Engineering A, vol. 527, pp. 7490–7497 (2010).

[101] *"Selective laser melting. Direct manufacturing of 3D-objects by selective laser melting of metal powders"*, Igor Yadroitsev, LAP LAMBERT Academic Publishing AG & Co. KG, (2009);

[102] Pierluigi Tozzi, Piergiorgio Stella, Iacopo Giovannetti, Massimiliano Buccioni, *"Heat Treatment Optimization for DMLM Ni-base Superalloy"*, in Additive Manufacturing and 3D printing International Conference, Nottingham 7-11 July 2014;

[103] L. Facchini Jr., N. Vicente, I. Lonardelli, E. Magalini, P. Robotti, A. Molinari; Advanced Engineering Materials, vol. 12, pp. 184–188, (2010).

Scientific Production

Congresses

1) **"Spark Plasma Sintering of a nickel-base superalloy"**,
P. Stella, M. Buccioni, A. Molinari
Proceedings EURO PM2013 Congress & Exhibition, Gotheborg 15-18 September 2013, ed. EPMA, Shrewsbury (UK), vol 1, p. 421-426

2) **"Heat Treatment Optimization for DMLM Ni-base Superalloy"**
Pierluigi Tozzi, Piergiorgio Stella, Iacopo Giovannetti, Massimiliano Buccioni
Proceedings of Additive Manufacturing and 3D printing International Conference, Nottingham 7-11 July 2014

3) "**Perspectives Of The Application Of High Strength Nickel Base Alloys by Hip in Rotating Equipment For Oil & Gas Industry"**
Gabriele Masi, Piergiorgio Stella, Massimo Giannozzi, Federico Iozzelli
Proceedings of HIP '14 - 11° International conference of Hot Isostatic Pressing, Stockholm 9-13 June 2014

Journals

1) **Microstructure and microhardness of heat-treated Ti–6Al–2Sn–4Zr–6Mo alloy**
Piergiorgio Stella, Iacopo Giovanetti, Gabriele Masi, Matteo Leoni, Alberto Molinari
Journal of Alloys and Compounds, Volume 567, 5 August 2013, Pages 134-140

2) **"Microstructure and mechanical properties of the P/M precipitation-hardening alloy N07626: effect of HIP temperature and solution annealing.",**
P. Stella, G. Masi, A. Molinari
submitted to Powder Metallurgy